

# T-PHOT<sup>\*</sup>: a new code for PSF-matched, prior-based, multiwavelength extragalactic deconfusion photometry

E. Merlin<sup>1</sup>, A. Fontana<sup>1</sup>, H. C. Ferguson<sup>2</sup>, J. S. Dunlop<sup>3</sup>, D. Elbaz<sup>4</sup>, N. Bourne<sup>3</sup>, V. A. Bruce<sup>3</sup>, F. Buitrago<sup>3,10,11</sup>, M. Castellano<sup>1</sup>, C. Schreiber<sup>4</sup>, A. Grazian<sup>1</sup>, R. J. McLure<sup>3</sup>, K. Okumura<sup>4</sup>, X. Shu<sup>4,8</sup>, T. Wang<sup>4,9</sup>, R. Amorín<sup>1</sup>, N. Cappelluti<sup>5</sup>, A. Comastri<sup>5</sup>, S. Derriere<sup>6</sup>, S. M. Faber<sup>7</sup>, and P. Santini<sup>1</sup>

- <sup>1</sup> INAF - Osservatorio Astronomico di Roma, Via Frascati 33, I - 00040 Monte Porzio Catone (RM), Italy e-mail: [emiliano.merlin@oa-roma.inaf.it](mailto:emiliano.merlin@oa-roma.inaf.it)
- <sup>2</sup> Space Telescope Science Institute, 3700 San Martin Drive, Baltimore, MD 21218, USA
- <sup>3</sup> SUPA<sup>\*\*</sup>, Institute for Astronomy, University of Edinburgh, Royal Observatory, Edinburgh, EH9 3HJ, U.K.
- <sup>4</sup> Laboratoire AIM-Paris-Saclay, CEA/DSM/Irfu - CNRS - Université Paris Diderot, CEA-Saclay, pt courrier 131, F-91191 Gif-sur-Yvette, France
- <sup>5</sup> INAF - Osservatorio Astronomico di Bologna, Via Ranzani 1, I - 40127, Bologna, Italy
- <sup>6</sup> Observatoire astronomique de Strasbourg, Université de Strasbourg, CNRS, UMR 7550, 11 rue de l'Université, F-67000 Strasbourg, France
- <sup>7</sup> UCO/Lick Observatory, University of California, 1156 High Street, Santa Cruz, CA 95064, USA
- <sup>8</sup> Department of Physics, Anhui Normal University, Wuhu, Anhui, 241000, China
- <sup>9</sup> School of Astronomy and Astrophysics, Nanjing University, Nanjing, 210093, China
- <sup>10</sup> Instituto de Astrofísica e Ciências do Espaço, Universidade de Lisboa, OAL, Tapada da Ajuda, PT1349-018 Lisbon, Portugal
- <sup>11</sup> Departamento de Física, Faculdade de Ciências, Universidade de Lisboa, Edifício C8, Campo Grande, PT1749-016 Lisbon, Portugal

Preprint online version: December 7, 2024

## Abstract

**Context.** The advent of deep multiwavelength extragalactic surveys has led to the necessity for advanced and fast methods for photometric analysis. In fact, codes which allow analyses of the same regions of sky observed at different wavelengths and resolutions are becoming essential to thoroughly exploit current and future data. In this context, a key issue is the *confusion* (i.e. blending) of sources in low resolution images.

**Aims.** We present T-PHOT, a publicly available software package developed within the ASTRODEEP project. T-PHOT is aimed at extracting accurate photometry from low resolution images, where the blending of sources can be a serious problem for the accurate and unbiased measurement of fluxes and colours.

**Methods.** T-PHOT can be considered as the next generation to TFIT, providing significant improvements over and above it and other similar codes (e.g. CONVPHOT). T-PHOT gathers data from a high resolution image of a region of the sky, and uses this information (source positions and morphologies) to obtain priors for the photometric analysis of the lower resolution image of the same field. T-PHOT can handle different types of datasets as input priors: namely, i) a list of objects that will be used to obtain cutouts from the real high resolution image; ii) a set of analytical models (as *.fits* stamps); iii) a list of unresolved, point-like sources, useful e.g. for far infrared wavelength domains.

**Results.** By means of simulations and analysis of real datasets, we show that T-PHOT yields accurate estimations of fluxes within the intrinsic uncertainties of the method, when systematic errors are taken into account (which can be done thanks to a flagging code given in the output). T-PHOT is many times faster than similar codes like TFIT and CONVPHOT (up to hundreds, depending on the problem and the method adopted), whilst at the same time being more robust and more versatile. This makes it an optimal choice for the analysis of large datasets. When used with the same parameter sets as for TFIT it yields almost identical results (albeit in a much shorter time), but in addition we show how the use of different settings and methods significantly enhances the performance.

**Conclusions.** T-PHOT proves to be a state-of-the-art tool for multiwavelength optical to FIR image photometry. Given its versatility and robustness, T-PHOT can be considered the preferred choice for combined photometric analysis of current and forthcoming extragalactic imaging surveys.

**Key words.** Galaxy, photometry, multiwavelength, software

## 1. Introduction

Combining observational data from the same regions of the sky in different wavelength domains has become common practice in the past few years (e.g. Agüeros et al. 2005; Obrić et al. 2006; Grogin et al. 2011, and many oth-

<sup>\*</sup> T-PHOT is publicly available for downloading from [www.astrodeep.eu/t-phot/](http://www.astrodeep.eu/t-phot/).

<sup>\*\*</sup> Scottish Universities Physics Alliance

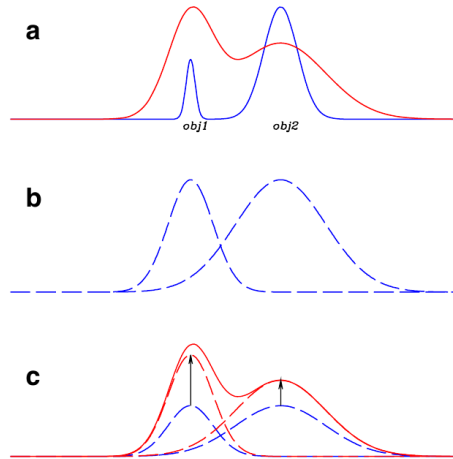


**Figure 1.** A schematic representation of the PSF-matched algorithm implemented in T-PHOT. Top: two objects are clearly detected and separated in the high resolution detection image (blue line). The same two objects are blended in the low resolution measurement image and have different colors (red line). Middle: the two objects are isolated in the detection image and are individually smoothed to the PSF of the measurement image, to obtain normalized model templates. Bottom: the intensity of each object is scaled to match the global profile of the measurement image. The scaling factors are found with a global  $\chi^2$  minimisation over the object areas. Image from De Santis et al. (2007).

ers). However, the use of both space-based and ground-based imaging instruments, with different sensitivities, pixel scales, angular resolutions, and survey depths, raises a number of challenging difficulties in the data analysis process.

In this context, it is of particular interest to obtain detailed photometric measurements for high redshift galaxies in the near infrared (NIR; corresponding to rest-frame optical) and far infrared (FIR) domains. In particular, great attention must be paid to bandpasses containing spectral features which allows for thorough physical investigation of the sources, to disentangle degenerate observational features and to obtain crucial clues to the understanding of the galactic physics (e.g. Daddi et al. 2004; Fontana et al. 2009). For example, at  $z > 3$  photometry longward of  $H$ -band is needed to locate and measure the size of the Balmer break. A passive galaxy at  $z \simeq 6$  (having the Balmer break lying longward of the  $K$ -band) can have  $H$  band and  $3.6\mu\text{m}$  fluxes compatible with e.g. a star forming, dusty galaxy at  $z \simeq 1$ , and  $K$ -band photometry is necessary to disentangle the degeneracy. However, the limited resolution of the ground based  $K$ -band observations can impose severe limits on the reliability of traditional aperture or even PSF-fitting photometry. Also, IRAC photometry is of crucial importance to obtain reliable photometric redshifts for red and high- $z$  sources, and to derive robust stellar mass estimates.

To address this, a high resolution image (HRI), obtained e.g. from the Hubble Space Telescope in the optical domain, can be used to retrieve detailed information on the positions and morphologies of the sources in a given region of the sky. Such information can be subsequently used to perform the photometric analysis of the lower resolution image (LRI), using the HRI data as priors. However, simply performing aperture photometry on the LRI at the positions measured in the HRI can be dramatically affected by neighbour contamination for reasonably sized apertures. On the other hand, performing source extraction on both images and matching the resulting catalogs is compro-

mised by the inability to deblend neighbouring objects, and may introduce significant inaccuracies in the cross-correlation process. PSF-matching techniques that degrade high-resolution data to match the low resolution data discard much of the valuable information obtained in the HRI, reducing all images to the “lowest common denominator” of angular resolution. Moreover, crowded-field, PSF-fitting photometry packages such as DAOPHOT (Stetson 1987) perform well if the sources in the LRI are unresolved, but are unsuitable for analysis of even marginally resolved images of extragalactic sources.

A more viable approach consists of taking advantage of the morphological information given by the HRI, to obtain high resolution cutouts or models of the sources. These priors can then be degraded to the resolution of the LRI using a suitable *convolution kernel*, constructed by matching the PSFs of the HRI and of the LRI. Such low resolution templates, normalized to unit flux, can then be placed at the positions given by the HRI detections, and the multiplicative factor that must be assigned to each model to match the measured flux in each pixel of the LRI will give the measured flux of that source. Such an approach, although relying on some demanding assumptions as described in the following Sections, has proven to be efficient. It has been implemented in such public codes as TFIT (Laidler et al. 2007) and CONVPHOT (De Santis et al. 2007), and has already been utilized successfully in previous studies (e.g. Guo et al. 2013; Galametz et al. 2013).

In this paper we describe a new software package, T-PHOT, developed at INAF-OAR as part of the ASTRODEEP project<sup>1</sup>. T-PHOT can be considered as a new, largely improved version of TFIT, supplemented with many of the features of CONVPHOT. Moreover, it adds many important

<sup>1</sup> ASTRODEEP is a co-ordinated and comprehensive program of i) algorithm/software development and testing; ii) data reduction/release, and iii) scientific data validation/analysis of the deepest multi-wavelength cosmic surveys. To get more information, visit <http://astrodeep.eu>.

new options, including the possibility of adopting different types of priors (namely, real images, analytical models, or point-sources). In particular, it is possible to use T-PHOT on FIR and sub-millimetric (sub-mm) datasets, as a competitive alternative to the existing dedicated software such as FASTPHOT (B  thermin et al. 2010) and DESPHOT (Roseboom et al. 2010; Wang et al. 2014). This makes T-PHOT a versatile tool, suitable for the photometric analysis of a very broad range of wavelengths from UV to sub-mm.

T-PHOT is a robust and easy-to-handle code, with a precise structural architecture (a PYTHON envelope calling C/C++ core codes) in which different routines are encapsulated, implementing various numerical/conceptual methods, to be chosen by simple switches in a parameter file. While a standard default “best choice” usage mode is provided and suggested, the user is allowed to select their own preferred way of obtaining their dataset.

One of the main advantages of T-PHOT is a significant saving of computational time with respect to both TFIT and CONVPHOT (see Sect. 5). This has been achieved with the use of fast C modules and an efficient structural arrangement of the code. In addition to this, we demonstrate how different choices of parameters influence the performance, and can be optimized to significantly improve the final results with respect to e.g. TFIT.

The plan of the paper is as follows. Sect. 2 provides a general introduction to the code, its mode of operation and its algorithms. In Sect. 3 some assumptions, limitations and caveats relative to the method are pointed out and discussed. Sect. 4 presents a comprehensive set of tests, based on both simulated and real datasets, to assess the performance of the code and to fully illustrate its capabilities and limitations. Sect. 5 briefly discusses the computational performances of T-PHOT and provides some reference computational timescales. Finally, in Sect. 6 the key features of T-PHOT are summarized, and outstanding issues and potential complications are briefly discussed.

## 2. General description of the code

As described above, T-PHOT uses spatial and morphological information gathered from a HRI to measure the fluxes in a LRI. To this aim, a linear system is built and solved via matricial computing, minimizing the  $\chi^2$  (in which the numerically determined fluxes for each detected source are compared to the measured fluxes in the LRI, summing the contributions of all pixels). Moreover, the code produces a number of diagnostic outputs and allows for an iterative re-calibration of the results. Fig. 1 shows a schematic depiction of the basic PSF-matched fitting algorithm used in the code.

As HRI priors T-PHOT can use i) real cutouts of sources from the HRI, ii) models of sources obtained e.g. with GALFIT or similar codes, iii) a list of coordinates where PSF-shaped sources will be placed; or a combination of these three types of priors.

For a detailed technical description of the mode of operation of the code, we refer the reader to the Appendix and to the documentation included in the downloadable tarball. Here, we will briefly describe its main features.

### 2.1. Pipeline

The pipeline followed by T-PHOT is outlined in the flowchart given in Fig. 2. The following paragraphs give a short description of the pipeline.

#### 2.1.1. Input

The input files needed by T-PHOT vary depending on the type(s) of priors used.

If “true” *high-resolution priors* are used, e.g. for optical/NIR ground-based or IRAC measurements using HST cutouts, T-PHOT needs:

- the detection, high resolution image (HRI) in `.fits` format;
- the catalog of the sources in the HRI, obtained e.g. using SEXTRACTOR or similar codes (the required format is described in Appendix A);
- the segmentation map of the HRI, in `.fits` format, again obtained e.g. using SEXTRACTOR or similar codes, having the value of the `id` of each source in the pixels belonging to it, and zero everywhere else;
- a convolution kernel  $K$ , in the format of a `.fits` image or of a `.txt` file, matching the PSFs of the HRI and the LRI so that  $PSF_{LRI} = K * PSF_{HRI}$  ( $*$  is the symbol for convolution). The kernel *must* have the HRI pixel scale.

If *analytical models priors* are used as priors (e.g. GALFIT models), T-PHOT needs:

- the stamps of the models (one per object, in `.fits` format);
- the catalog of the models (the required format is described in Appendix A);
- the convolution kernel  $K$  matching the PSFs of the HRI and the LRI, as in the previous case.

If models have more than one component, one separate stamp per component, and catalogs for each component are needed (e.g. one catalog for bulges and one catalog for disks).

If *unresolved, point-like priors* are used, T-PHOT needs:

- the catalog of positions (the required format is described in Appendix A);
- the LRI PSF, in the LRI pixel scale.

In this case, a potential limitation to the reliability of the method is given by the fact that the prior density usually needs to be optimised with respect to FIR/sub-mm maps, as discussed e.g. in Shu et al. (2015, in preparation) and Elbaz et al. (2011) (see also Wang et al. 2015; Bourne et al. 2015, in preparation). The optimal number of priors turns out to be around 50-75% of the numbers of beams in the map. The key problem is to identify which of the many potential priors from e.g. an HST catalogue one should use. This is a very complex issue and we do not discuss it in this paper.

If mixed priors are used, T-PHOT obviously needs the input files corresponding to each of the different types of priors in use.

Finally, in all cases T-PHOT needs

- the measure LRI, *background subtracted* (see next paragraph), in `.fits` format, with the same orientation as

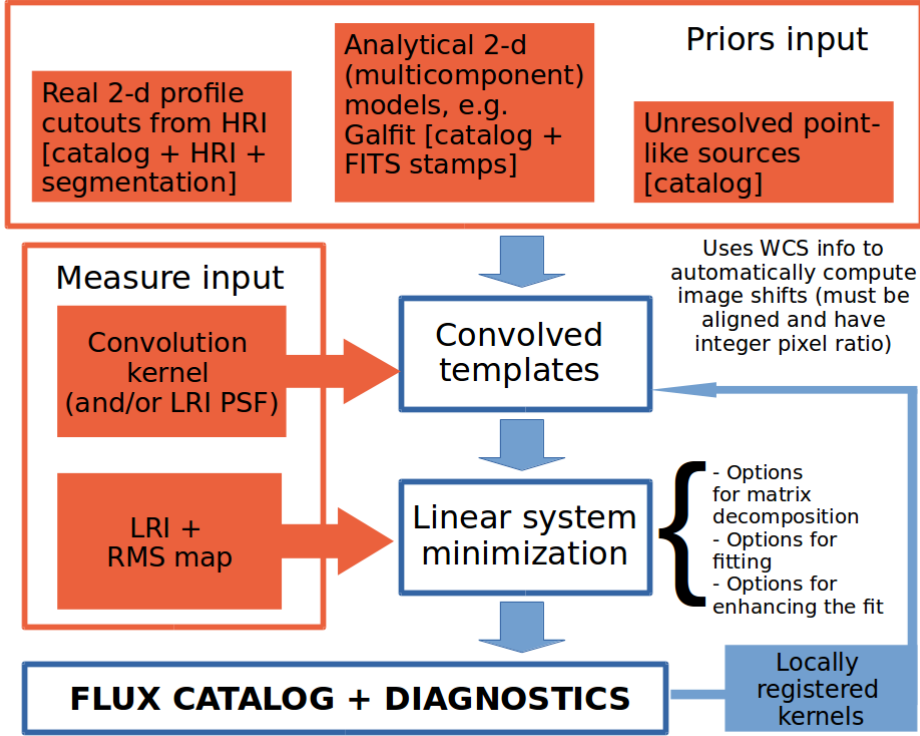


**Figure 2.** Schematic representation of the workflow in T-PHOT.

the HRI (i.e., no rotation allowed); the pixel scale can be equal to, or an integer multiple of, the HRI pixel scale, and the origin of one pixel must coincide; it should be in surface brightness units (e.g. counts/s/pixel, or Jy/pixel for FIR images, and not PSF-filtered);

- the LRI RMS map, in `.fits` format, with the same dimensions and WCS of the LRI.

Table 1 summarizes the input requirements for the different choices of priors just described.

All the input images *must* have the following keywords in their headers: `CRPIXn`, `CRVALn`, `CDn_n`, `CTYPEn` ( $n=1,2$ ).

### 2.1.2. On the background subtraction

As already mentioned, the LRI *must* be background subtracted before being fed to T-PHOT. This is of particular interest when dealing with FIR/sub-mm images, where the typical standard is to use zero-mean. To estimate the background level in optical/NIR images, one simple possibility is to take advantage of the option to fit point-like sources to measure the flux for a list of positions chosen to fall within void regions. The issue is more problematic in such confusion-limited FIR images where there are no empty sky regions. In such cases, it is important to separate the fitted sources (those listed in the prior catalogue) from the background sources, which contribute to a flat background level behind the sources of interest. The priors should be chosen so that these two populations are uncorrelated. The average contribution of the faint background source population can then be estimated e.g. by (i) injecting fake sources into the map and measuring the average offset (output-input) flux; or (ii) measuring the modal value in the residual im-

age after a first pass through T-PHOT (see e.g. Bourne et al. 2015, in preparation).

### 2.1.3. Stages

T-PHOT goes through “stages”, each of which performs a well defined task. The best results are obtained performing two runs (“pass 1” and “pass 2”), the second one using locally registered kernels, produced during the first one. The possible stages are the following:

- **priors**: creates/organizes stamps for sources as listed in the input priors catalog(s);
- **convolve**: convolves each high resolution stamp with the convolution kernel  $K$  to obtain models (“templates”) of the sources at LRI resolution. *The templates are normalized to unit total flux.* If the pixel scale of the images is different, transforms templates accordingly. Convolution is preferably performed in Fourier space, using fast `FFTW3` libraries; however the user can choose to perform it in real pixel space, ensuring a more accurate result at the expense of a much slower computation.
- **positions**: if an input catalog of unresolved sources is given, creates the PSF-shaped templates listed in it, and merges it with the one produced in the **convolve** stage;
- **fit**: performs the fitting procedure, solving the linear system and obtaining the multiplicative factors to match each template flux with the measured one;
- **diags**: selects the best fits<sup>2</sup> and produces the final formatted output catalogs with fluxes and errors, plus some other diagnostics, see Sect. 2.3;

<sup>2</sup> Each source is fitted more than once if an arbitrary grid is used, as in the standard `TFIT` approach.

	Real cutouts	Analytical models	Point-sources
Priors	HRI Segmentation Catalog	HRI Model Stamps Catalog	Positions Catalog
Transformation	Convolution Kernel	Convolution Kernel	PSF <sub>LRI</sub>
Measure	LRI RMS <sub>LRI</sub>	LRI RMS <sub>LRI</sub>	LRI RMS <sub>LRI</sub>

**Table 1.** The input files needed by T-PHOT for different settings. See text for details.

- **dance**: obtains local convolution kernels for the second pass; it can be skipped if the user is only interested in a single pass run;
- **plotdance**: plot some diagnostics for the dance stage; it can be skipped for any other purpose than diagnostics;
- **archive**: archives all results in a subdirectory whose name is based on the LRI and the chosen fitting method (to be only used at the end of the second pass).

The exact pipeline followed by the code is specified by a keyword in the input parameter file. See the Appendix for a more detailed description of the whole procedure.

#### 2.1.4. Solution of the linear system

The search for the LRI fluxes of the objects detected in the HRI is performed by creating a linear system

$$\sum_{m,n} I(m,n) = \sum_{m,n} \sum_i^N F_i P_i(m,n) \quad (1)$$

where  $m$  and  $n$  are the pixel indexes,  $I$  contains the pixel values of the fluxes in the LRI,  $P_i$  is the normalized flux of the template for the  $i$ -th objects in the (region of the) LRI being fitted, and  $F_i$  is the multiplicative scaling factor for each object. In physical terms,  $F_i$  represent the flux of each object in the LRI (that is, it is the unknown to be determined).

Once the normalized templates for each object in the (region of interest within the) LRI have been generated during the `convolve` stage, the best fit to their fluxes can be simultaneously derived by minimizing a  $\chi^2$  statistic,

$$\chi^2 = \left[ \frac{\sum_{m,n} I(m,n) - M(m,n)}{\sigma(m,n)} \right]^2 \quad (2)$$

where  $m$  and  $n$  are the pixel indexes,

$$M(m,n) = \sum_i^N F_i P_i(m,n) \quad (3)$$

and  $\sigma$  is the value in the  $(m,n)$  pixel of the RMS map.

The output quantities are the best-fit solutions of the minimization procedure, i.e. the  $F_i$  parameters and their relative errors. They can be obtained resolving the linear system

$$\frac{\partial \chi^2}{\partial F_i} = 0 \quad (4)$$

for  $i = 0, 1, \dots, N$ .

In practice, the linear system can be rearranged into a matrix equation,

$$AF = B \quad (5)$$

where the matrix  $A$  contains the coefficients  $P_i P_j / \sigma^2$ ,  $F$  is a vector containing the fluxes to be determined, and  $B$  is a vector given by  $I_i P_i / \sigma^2$  terms. The matrix equation is solved via one of three possible methods as described in the next subsection.

#### 2.1.5. Fitting options

T-PHOT allows for some different options to perform the fit:

- three different methods for solving the linear system are implemented: namely, the LU method (used by default in `TFIT`); the Cholesky method; and the Iterative Biconjugate Gradient method (used by default in `CONVPHOT`; for a review on methods to solve sparse linear systems see e.g. Davis 2006). They prove to yield similar results, the LU method being slightly more stable and faster;
- a threshold can be imposed so that only pixels with a flux higher than it will be used in the fitting procedure (see Sect. 4.1.4);
- sources fitted with a large, unphysical negative flux ( $f_{meas} < -3\sigma$ , where  $\sigma$  is their nominal error, see below) can be excluded from the fit, and in this case a new fitting loop will be performed without considering these sources.

The fit can be performed (i) on the entire LRI as a whole, producing a single matrix containing all the sources (this is the method adopted in `CONVPHOT`); (ii) subdividing the LRI into an arbitrary grid of (overlapping) small cells, performing the fit in each of such cells separately, and then choosing the “best” fit for each source, using some convenient criteria to select it (because sources will be fitted more than once, if the cells overlap. This is the method adopted in `TFIT`); (iii) ordering objects by decreasing flux, building a cell around each source including all its potential contaminants, solving the problem in that cell and assigning to the source the obtained flux (*cells-on-objects* method; see the Appendix for more details).

While the first method is the safest and more accurate because it does not introduce any bias or arbitrary modifications, it may often be unfeasible to process at once large or very crowded images. Potentially large computational time saving is possible using the *cells-on-objects* method, depending on the level of blending/confusion in the LRI: if the latter is very high, most sources will be overlapping, so the cells will end up being very large. This ultimately results in repeating many times the fit on regions with dimensions comparable to the whole image (a check is implemented in the code, to automatically change the method from *cells-on-objects* to single fit if this is the case). If the confusion is not dramatic, a saving in computational time

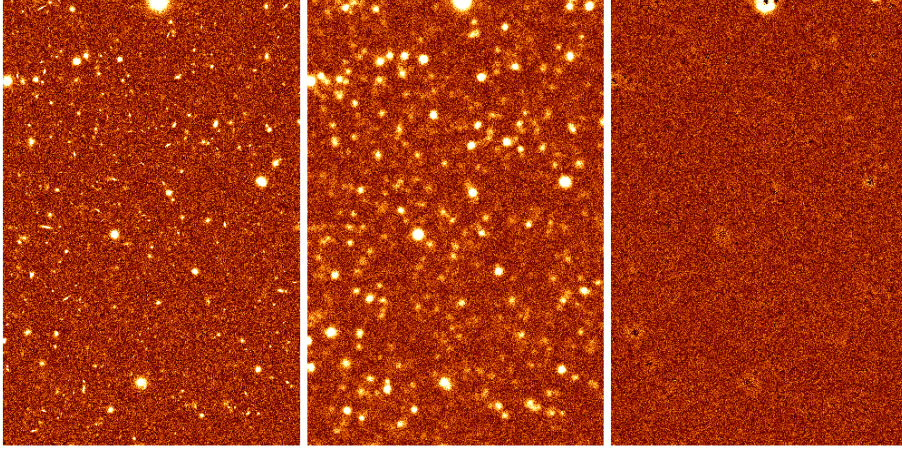


**Figure 3.** Example of the results of a standard T-PHOT run using extended priors. Left to right: HRI (FWHM=0.2''), LRI (FWHM=1.66''), and residuals image for a simulated dataset. LRI and residual image are on the same grayscale.

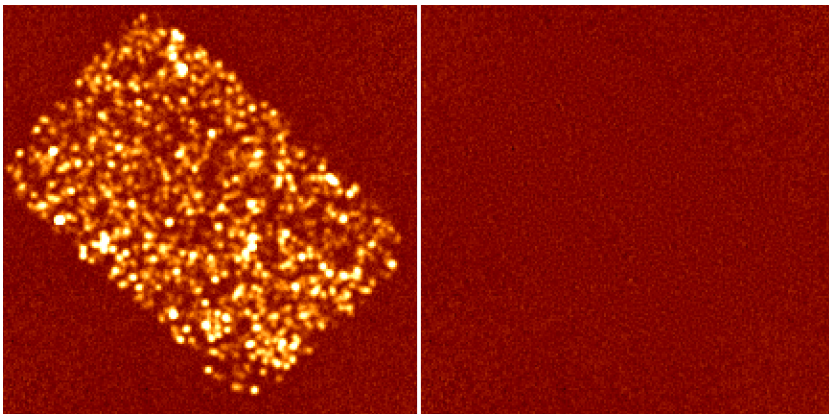


**Figure 4.** Example of the results of a standard T-PHOT run using point-source priors. Left to right: LRI (FWHM=25'') and residuals image (same grayscale) for a simulated dataset. See also Sect. 4.1.2.

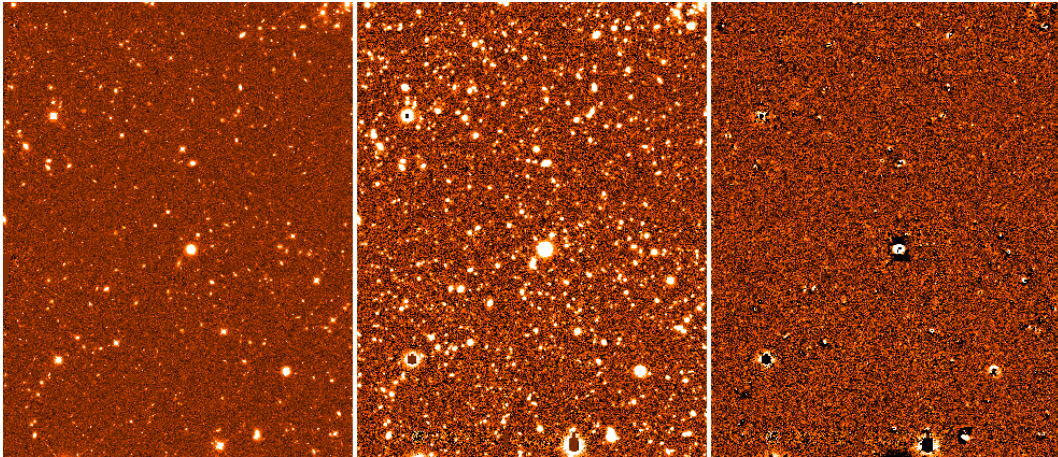


**Figure 5.** Example of the results of a standard T-PHOT run using analytical priors. Left to right: CANDELS COSMOS *H*-band (HRI), *R*-band (LRI) and residuals image obtained using GALFIT two-component models. LRI and residual image are on the same grayscale.

up to two orders of magnitude can be achieved. The results obtained using the *cells-on-objects* method prove to be virtually identical to those obtained with a single fit on the whole image (see Sect. 4.1.2). On the other hand, using the arbitrary cells method is normally the fastest option, but can introduce potentially large errors to the flux estimates,

due to wrong assignments of peripheral flux from sources located outside a given cell to sources within the cell (again, see Sect. 4.1.2 and Appendix).

### 2.1.6. Post-fitting stages: kernel registration

After the fitting procedure is completed, T-PHOT will produce the final output catalogs and diagnostic images (see 2.3). Among these, a *model* image is obtained by adding all the templates, scaled to their correct total flux after fitting, in the positions of the sources. This image will subsequently be used if a second pass is planned, during a stage named **dance**: a list of positional shifts is computed, and a set of shifted kernels are generated and stored. The **dance** stage consists of three conceptual steps:

- the LRI is divided into cells of given size (specified by the keyword `dzonesize`) and a linear  $\Delta x, \Delta y$  shift is computed within each cell, cross-correlating the model image and the LRI in the considered region<sup>3</sup>;
- interpolated shifts are computed for the regions where the previous registration process gives spuriously large shifts, i.e. above the given input threshold parameter `maxshift`;
- the new set of kernels is created using the computed shifts to linearly interpolate their positions, while catalogs reporting the shifts and the paths to kernels are produced.

### 2.1.7. Second pass

The registered kernels can subsequently be used in the second pass run, to obtain more astrometrically precise results. T-PHOT automatically deals with them provided the correct keyword is given in the parameter file. If unresolved priors are used, the list of shifts generated in the **dance** stage will be used by the `positions` routine during the second pass to produce correctly shifted PSFs and generate new templates.

## 2.2. Error budget

During the fitting stage, the covariance matrix is constructed and output. Errors for each source are assigned as the square root of the diagonal element of the covariance matrix relative to that source. It must be pointed out that using any cell method for the fitting, rather the single fitting option, will affect this uncertainty budget, since a different matrix will be constructed and resolved in each cell.

It is important to stress that this covariance error budget is a *statistical* uncertainty, relative to the RMS fluctuations in the measurement image, and is not related to any possible *systematic* error. The latter can instead be estimated by flagging potentially problematic sources, to be identified separately from the fitting procedure. There can be different possible causes for systematic offsets of the measured flux with respect to the true flux of a source. T-PHOT assigns the following flags:

- +1 if the prior has saturated or negative flux;
- +2 if the prior is blended (the check is performed on the segmentation map);
- +4 if the source is at the border of the image (i.e. its segmentation reaches the limits of the HRI pixels range).

<sup>3</sup> FFT and direct cross-correlations are implemented, the latter being the preferred default choice because it gives more precise results at the expense of a slightly slower computation.

## 2.3. Description of the output

T-PHOT output files are designed to be very similar in format to those produced by TFIT. They provide:

- a “best” catalog containing the following data, listed for each detected source (as reported in the catalog file header):
  - `id`;
  - `x` and `y` positions (in LRI pixel scale and reference frame, FITS convention where first pixel is centered at 1,1);
  - `id` of the cell in which the best fit has been obtained (only relevant for arbitrary grid fitting method);
  - `x` and `y` positions of the object in the cell and distance from the center (always equal to 0 if the *cells-on-objects* method is adopted);
  - fitted flux and its uncertainty (square root of the variance, from the covariance matrix). These are the most important output quantities;
  - flux of the object as given in the input HRI catalog or, in the case of point-sources priors, measured flux of the pixel at the `x, y` position of the source in the LRI;
  - flux of the object as determined in the `cutout` stage (it can be different to the previous one, e.g. if the segmentation was dilated); in case of point-sources priors, measured flux of the pixel at the `x, y` position of the source in the LRI;
  - `flag` indicating a possible bad source as described in the previous subsection;
  - number of fits for the object (only relevant for arbitrary grid fitting method, 1 in all other cases).
  - `id` of the object having the largest covariance with the present source;
  - `covariance index`, i.e. the ratio of the maximum covariance to the variance of the object itself; this number can be considered an indicator of the reliability of the fit, since large covariances often indicate a possible systematic offset in the measured flux of the covarying objects (see Sect. 4.1.2).
- two catalogs reporting statistics for the fitting cells and the covariance matrices (they are described in the documentation);
- the model `.fits` image, obtained as a collage of the templates, as already described;
- a diagnostic residual `.fits` image, obtained by subtracting the model image from the LRI;
- a subdirectory containing all the low resolution model templates;
- a subdirectory containing the covariance matrices in graphic (`.fits`) format;
- a few ancillary files relating to the shifts of the kernel for the second pass and a subdirectory containing the shifted kernels.

All fluxes and errors are output in units consistent with the input images.

Figs. 3, 4 and 5 show three examples of T-PHOT applications on simulated and real data, using the three different options for priors.

### 3. Assumptions and limitations

The PSF-matching algorithms implemented in T-PHOT and described in the previous section are prone to some assumptions and limitations. In particular, it must be pointed out that:

- the accuracy of the results strongly depends on the reliability of the determined PSFs (and consequently of the convolution kernel). A few percent error in the central slope of the PSF light profile might lead to non-negligible systematical deviations in the measured fluxes. However, it should be pointed out that in principle, since the fitting algorithm minimizes the residuals on the basis of a summation on pixels, some effect of compensation effect should take place: for example, if the PSF is too shallow the fitting algorithm will probably remove too much light in the central regions, but it will compensate this by leaving a corresponding amount of light in the outskirts, so that the global determined flux should be close to the correct one even in presence of such systematic morphological deviations. Typical patterns in the residual images can help highlighting such a trend (see Fig. 6);

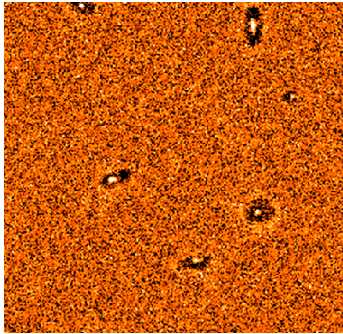


**Figure 6.** Typical patterns in a residual image created by T-PHOT, caused by inaccurate PSF/kernel determination. In this case, the ring-shaped shadow surrounding a bright central spot is due to an underestimation of the central peak of the LRI PSF, which causes an overestimation of the fit in the outskirts while leaving too much light in the center.

- when dealing with extended priors, it is assumed that the intrinsic morphology of the objects does not change with the wavelength. Of course, this is usually not the case. The issue is less of a problem when dealing with FIR images having unresolved priors, because the morphology of the objects usually becomes irrelevant with respect to the PSF features at such long wavelengths. On the other hand, for what concerns the optical and NIR domains, a possible way to solve the problem could be the use of multi-component analytical models as priors. In this approach, each component should be fitted independently, thus letting the ratio between e.g. a bulgy and a disk component free to vary from the HRI to the LRI. A clear cost of this approach is that any fail in the fit of irregular or difficult morphological features (spiral arms, blobs, asymmetries etc.) would be propagated in the convolution of the priors. This functionality is already implemented in T-PHOT and detailed testing on its real reliability is ongoing;

- as explained in Sect. 2.2, T-PHOT flags priors which clearly appear to be flawed: sources too close to the borders of the image, saturated objects, and most notably *blended priors*. The assumption that all priors are well separated from one another is crucial, and the method proves to fail when this requirement is not accomplished. Again, this is crucial only when dealing with real priors, while analytical models and unresolved priors do not suffer from this limitation;
- As anticipated in Sect. 2.1.1, FIR images can suffer from an “overfitting” problem, due to the presence of too many priors in each LRI beam if the HRI is deeper than the LRI. In this case, a selection of the priors based on some additional criteria (e.g., flux prediction from SED fitting) might be necessary to avoid catastrophic outcomes (see also Wang et al. 2015; Bourne et al. 2015, in preparation).

### 4. Validation

To assess the performance of T-PHOT we set up an extensive set of simulations, aimed at various different and complementary goals.

We used SKYMAKER (Bertin 2009), a public software tool, to build synthetic `.fits` images. The code ensures direct control on all the observational parameters (the magnitude and positions of the objects, their morphology, the zero point magnitude, the noise level, and the PSF). Model galaxies are built by summing a de Vaucouleurs and an exponential light profile in order to best mimic a realistic distribution of galaxy morphologies. These models are generated using a variety of bulge-to-total light ratios, component sizes and projection angles.

All tests have been run using ideal (i.e. synthetic and symmetric) PSFs and kernels.

Moreover, we also perform tests on real datasets taken from the CANDELS survey (in these cases using real PSFs).

Some of the tests were performed using both T-PHOT and TFIT, to cross-check the results, ensuring the perfect equivalency of the results given by the two codes when used with the same parameter sets, and showing how appropriate settings of the T-PHOT parameters can ensure remarkable improvements.

For simplicity, here we only show the results from a restricted selection of the tests dataset, which are representative of the performance of T-PHOT in standard situations. The results on the other simulations globally resemble the one we present, and are omitted for the sake of conciseness.

#### 4.1. Code performance and reliability on simulated images

##### 4.1.1. Basic tests

As a first test, we checked the performance of the basic method by measuring the flux of two PSF-shaped synthetic sources, with varying separation and signal to noise ratios. One hundred realizations with different noise maps of each parameter set were prepared, and the averages on the measured fluxes were computed. The aim of this test was twofold: on the one hand, to check the precision to which the fitting method can retrieve “true” fluxes in the simplest possible case - two sources with ideal PSF shape; on the other hand, to check the reliability of the nominal error budget given by the covariance matrix, comparing it to the

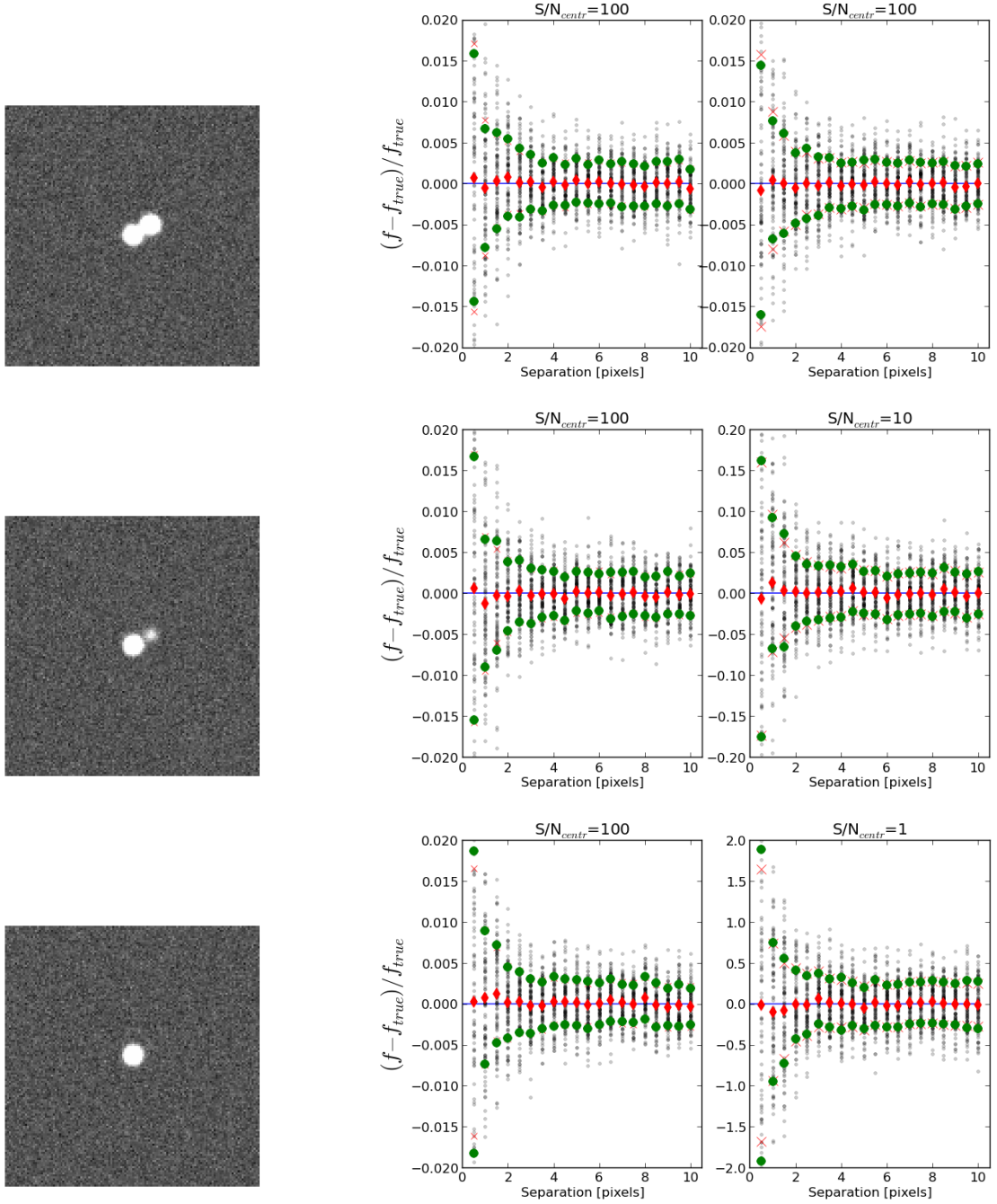


**Figure 7.** Accuracy check on idealized PSF-shaped objects. 100 realizations of the same image containing two PSF-shaped objects at varying positions and signal-to-noise ratios have been produced and the fluxes have been measured with T-PHOT. In each row, the left image shows one of the 100 realizations with the largest considered separation (10 pixels). On the right, the first panel refers to the central object, and the second (on the right) to the shifted object; central signal-to-noise ( $S/N_{centr}$ ) ratios are, from top to bottom, 100-100, 100-10, and 100-1 for the two objects respectively. In each panel, as a function of the separation interval between the two sources the faint grey points show each of the 100 flux measurements (in relative difference with respect to the “true” input flux), the red diamonds are the averages of such 100 measurements, the red crosses show the nominal error given by the covariance matrix in T-PHOT and the green dots the standard deviation of the 100 measurements. See text for more details.

real RMS of the 100 measurements. Fig. 7 shows three examples of the setup and the results of this test. Clearly, in both aspects the results are reassuring: the average of the 100 measurement (red diamonds) is always in very good agreement with the “true” value, with offset in relative error always well under the  $1/(S/N)_{centr}$  limit ( $(S/N)_{centr}$  is

the value of the signal to noise ratio in the central pixel of the source, corresponding to roughly one third of the total  $S/N$ ); and the nominal error (red crosses) given by the covariance matrix is always in good agreement with the RMS of the 100 measurements (red circles).

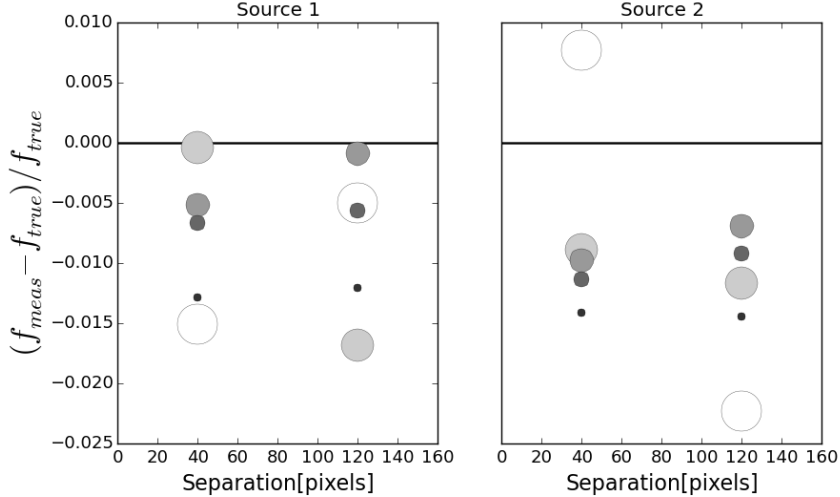


**Figure 8.** Effects of different segmentation areas on the measured flux of two isolated objects (each panel referring to one of the sources) having identical flux and signal-to-noise ratio (for each object, two cases with different relative separations of 40 and 120 pixels are considered and plotted). The shades and dimensions of the dots is a function of the radius of the segmentation, with darker and smaller dots corresponding to smaller segmentations. See text for more details.

When dealing with extended objects rather than with point-like sources, one must consider the additional problem that the entire profile of the source cannot be measured exactly, because the segmentation is limited by the lowest signal-to-noise isophote. The extension of the segmentation therefore comes to play a crucial role and defining it correctly is a very subtle issue. Simply taking the isophotal area as reported by SEXTRACTOR as ISOAREA often underestimates the real extension of the objects. Accordingly, the segmentation of the sources should somehow be enlarged to include the faint wings of sources. To this aim, specific software called DILATE has been developed at OAR and used in the CANDELS pipeline for the photometric analysis of GOODS-S and UDS IRAC data (Galametz et al. 2013). DILATE enlarges the segmentation by a given factor, depending on the original area; it has proven to be reasonably robust in minimizing the effects of underestimated segmented areas.

Fig. 8 shows the effects of artificially varying the dimensions of the segmentation relative to two bright, extended and isolated sources in a simulated HRI, on the flux measured for that source in a companion simulated LRI. Note how enlarging the segmented area normally results in larger measured fluxes, because more and more light from the faint wings of the source are included in the fit. However, beyond a certain limit the measurements begin to lose accuracy due to the inclusion of noisy, too low signal-to-noise regions (which may cause a lower flux measurement).

In principle, using extended analytical models rather than real high resolution cutouts should cure this problem more efficiently, because models have extended wings which are not signal-to-noise limited. Tests are ongoing to check the performance of this approach, and will be presented in a forthcoming paper.

#### 4.1.2. Tests on realistic simulations

The next tests were aimed at investigating less idealized situations, and have been designed to provide a robust analy-

sis of the performance of the code on realistic datasets. We used the code GENCAT (Schreiber et al. 2015, in preparation) to produce mock catalogs of synthetic extragalactic sources, with reasonable morphological features and flux distribution<sup>4</sup>. Then, a set of images were produced using such catalogs as an input for SKYMAKER. A “detection” HRI mimicking an HST H band observation (FWHM = 0.2”) was generated from the GENCAT catalog, using output parameters to characterize the objects’ extended properties. Then a set of measure LRI’s were produced: a first one was populated with PSF-shaped sources, having FWHM = 1.66” (the typical IRAC-ch1/ch2 resolution, a key application for T-PHOT), while other LRIs were created from the input catalog, mimicking different ground-based or IRAC FWHMs. Finally, we created another HRI catalog removing all of the overlapping sources<sup>5</sup>. This “non-overlapping” catalog was used to create parallel detection and measurement images, to obtain insight into the complications given by the presence of overlapping priors. In all these images, the limiting magnitude was set equal to the assigned zero point, so that the limiting flux at  $1\sigma$  is 1.

<sup>4</sup> GENCAT is another software package developed within the ASTRODEEP project. It uses GOODS-S CANDELS statistics to generate a realistic distribution of masses at all redshifts, for two populations of galaxies (active and passive), consistently with observed mass functions. All the other physical properties of the mock galaxies are then estimated using analytical recipes from literature: each source is assigned a morphology (bulge to total ratio, disk and bulge scale lengths, inclination etc.), star formation rate, attenuation, optical and infrared rest-frame and observed magnitudes. Each source is finally assigned a sky-projected position mimicking the clustering properties of the real CANDELS data.

<sup>5</sup> We proceeded as follows. First, we created a “true” segmentation image using the input catalog and assigning to each object all the pixels in which the flux was  $1.005 \times f_{background}$ . Then, starting from the beginning of the list, we included each source in the new catalog if its segmented area did not overlap the segmented area of another already inserted source.

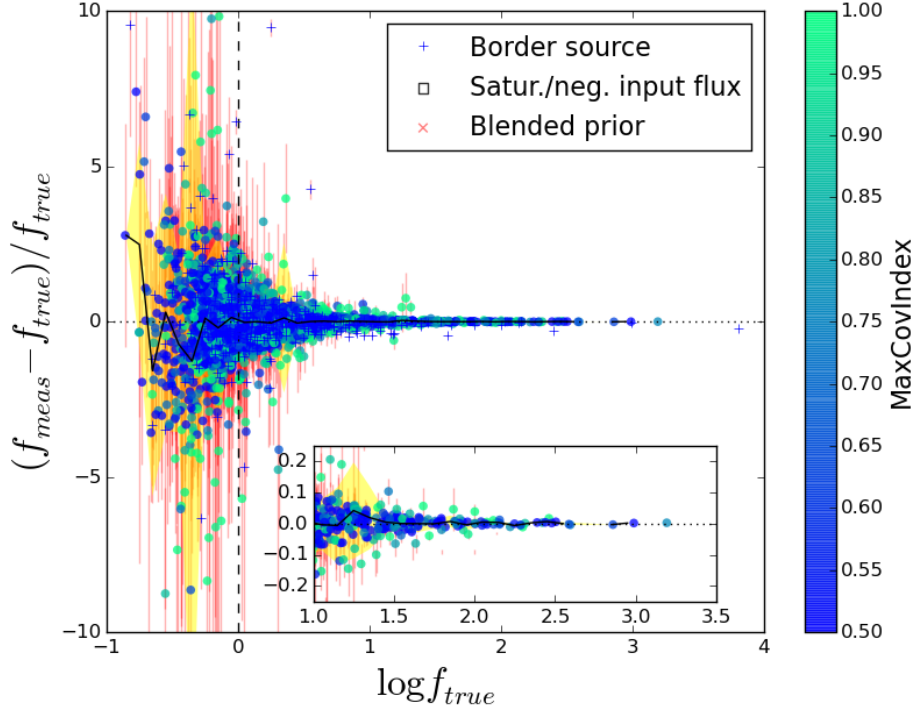


**Figure 9.** Accuracy of the flux determination in a simulation containing non-overlapping, PSF-shaped sources and “perfect” detection. Relative measured flux difference  $(f_{meas} - f_{true})/f_{true}$  is plotted versus logarithm of the input flux  $f_{true}$ , for a simulated image populated with PSF-shaped sources (FWHM=1.66”). Each dot corresponds to a single source, with different symbols and colors referring to various diagnostics as explained in the legend and in the colorbar. The black solid line is the average in bins, the yellow shade is the standard deviation. The vertical dashed line shows the limiting flux at  $1\sigma$ ,  $f = 1$ . The inner panel shows a magnification of the brighter end of the distribution. The fit has been performed on the whole image at once. See text for more details.

Also, the fits were always performed on the LRI as a whole, if not otherwise specified.

Fig. 9 shows the results relative to the first test, i.e. the fit on the image containing non-overlapping, PSF-shaped sources, with a “perfect” detection (i.e. the prior catalog contains all sources above the “true” detection limit), obtained with a single fit on the whole image. The figure shows the relative error in the measured flux of the sources,  $(f_{meas} - f_{true})/f_{true}$ , versus the log of the real input flux  $f_{true}$ ; the different symbols refer to the flag assigned to each object, while the color is a proxy for the covariance index, as described in more detail in the next paragraph.

In this case, the only source of uncertainty in the measurement is given by the noise fluctuations, which clearly becomes dominant in the faint end of the distribution. Looking at the error bars of the sources, which are given by the nominal error assigned by T-PHOT from the covariance matrix, one can see that almost all sources have measured flux within  $2\sigma$  from their “true” flux, with only strongly covariant sources (covariance index  $\simeq 1$ , greener colors) having  $|f_{meas} - f_{true}|/f_{true} > 1\sigma$ . The only noticeable exceptions are sources that have been flagged as potentially unreliable, as described in Sect. 2.2. Also note how the average  $\Delta f/f$  (solid black line) is consistent with zero down to  $f_{true} = S/N \simeq 0.63$ .

Fig. 10 shows the analysis of a case study in which the fluxes of a clump of highly covariant objects are measured with poor accuracy, and some of the nominal uncertainties

are underestimated: a very bright source (ID 3386,  $m_{true} = 21.17$ ) shows a relative difference  $(f_{meas} - f_{true})/f_{true} > 3\sigma$ . To cast light on the reason for such a discrepancy, the region surrounding the object was replicated 100 times with different noise realizations, and the results were analyzed and compared. The upper panels show (left) one of the 100 measurement images and (right) the position of all the sources in the region (many of which are close to the detection limit). The color code refers to the covariance index of the sources. The bottom left panel shows the relative error in the measured flux for all the sources in the region, with the inner panels showing magnifications relative to the object ID 3386 and to the bunch of objects with  $m_{true} \sim 26.5$ . Looking at the colors of their symbols, many objects in the region turn out to be strongly covariant. Indeed, while the “bluer” sources in the upper part of the region all have covariant indexes lower than 0.5, the “greener” ones in the crowded lower part all have covariance index larger than 1 (indeed larger than 2 in many cases). This means that their flux measurements are subject to uncertainties not only from noise fluctuations, but also from systematic errors due to their extremely close and bright neighbors. As clearly demonstrated here, the covariance index can give a clue about which measurements can be safely trusted.

The bottom right panel gives the sum of the measured fluxes of all sources in each of the 100 realizations (the blue line is the true total flux and the red line is the mean of the 100 measured total fluxes). It can be seen that the total

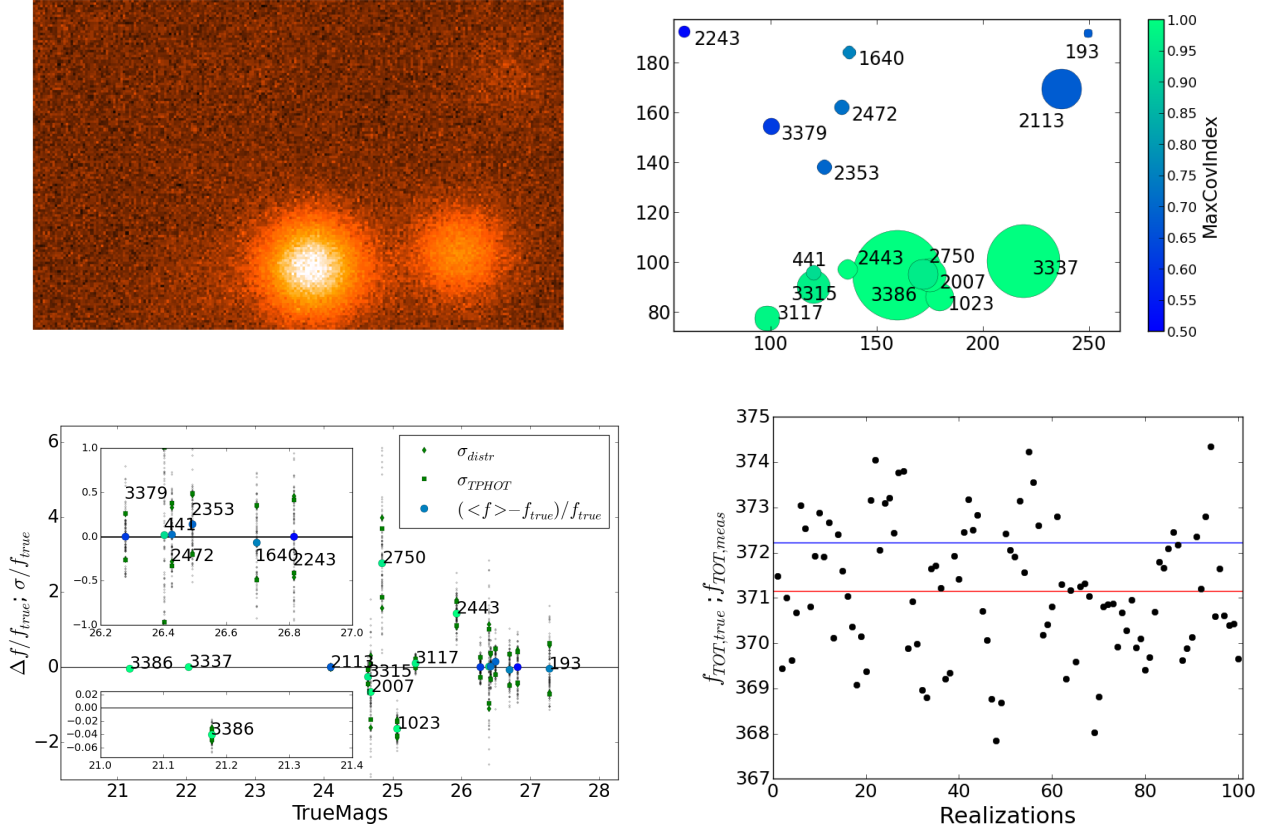


**Figure 10.** Analysis of a small region including a strongly covarying group of sources. Upper left panel: one of the 100 realizations with different noise maps of the region. Upper right panel: “true” spatial position of all the sources in the region (the color of the dots refer to the covariance index of the sources, as indicated in the colorbar, while their size is proportional to their true flux). Bottom left panel: relative deviation of measured flux from the true flux for each source in the region, as a function of their true magnitude (big dots show the average relative deviation, and their colors refer to their covariance index as in the previous panel; green squares show the nominal uncertainty given by T-PHOT, to be compared with the RMS of the distribution of the 100 measurements (diamonds); small grey dots are the single 100 measurements. Small inner panels show magnifications of regions of interest). Bottom right panel: each dot shows the sum of the measured fluxes for each of the 100 realizations, and the average of this sum (red line) to be compared with the “true” sum (blue line), showing that an overall consistency is guaranteed by the method. See text for more details.

flux measured in the region is always consistent with the expected true one to within  $\simeq 1\%$  of its value.

The bottom line of this analysis is that, although it is not possible to postulate a one-to-one relation (because in many cases sources having a large covariance index have a relatively good flux estimate, see Fig. 9), the covariance index, together with the flagging code outputted by T-PHOT, can give clues about the reliability of measured flux, and should be taken into consideration during the analysis of the data. Measurements relative to sources having covariance index e.g. larger than 1 should be treated with caution.

In a subsequent more realistic test, we considered extended objects (including morphologies of objects from the GENCAT catalog, using  $\text{FWHM}_{HRI}=0.2''$  and  $\text{FWHM}_{LRI}=1.66''$  and imposing  $m_{true,LRI}=m_{true,HRI} = m_{H160,GenCat}$  for simplicity) and allowed for overlapping priors. To be consistent with the standard procedure adopted for real images, for this case we proceeded by producing an SEXTRACTOR catalog and segmentation map, which were then spatially cross-correlated with the “true” input catalog. The results for this test are shown in Fig. 11. Even in this much more complex situation, the results are reassuring: there is an overall good agreement be-

tween measured and input fluxes for bright ( $\log S/N > 1$ ) sources, with only a few flagged objects clearly showing large deviations from the expected value, and a reasonably good average agreement down to  $\log S/N = 0$ . However, all bright fluxes are measured  $\simeq 5\%$  fainter than the true values (see the inner box in the same Figure); this is very likely to be the effect of the limited segmentation extension, as already discussed in the previous Section. On the other hand, faint sources tend to have systematically over-estimated fluxes, arguably because of contamination from undetected sources. To confirm this, we focus our attention on a single case study (the source marked as ID 720) which shows a large discrepancy from its true flux, but has a relatively small covariance index. An analysis of the real segmentation map shows how in reality the detected object is a superposition of two different sources, which have been detected as a single one, so that the measured flux is of course higher than expected. One should also note that the uncertainties on the measured fluxes are smaller in this test, because there are fewer priors (only the ones detected by SEXTRACTOR are now present), implying a lower rank of the covariance matrix and a lower number of detected

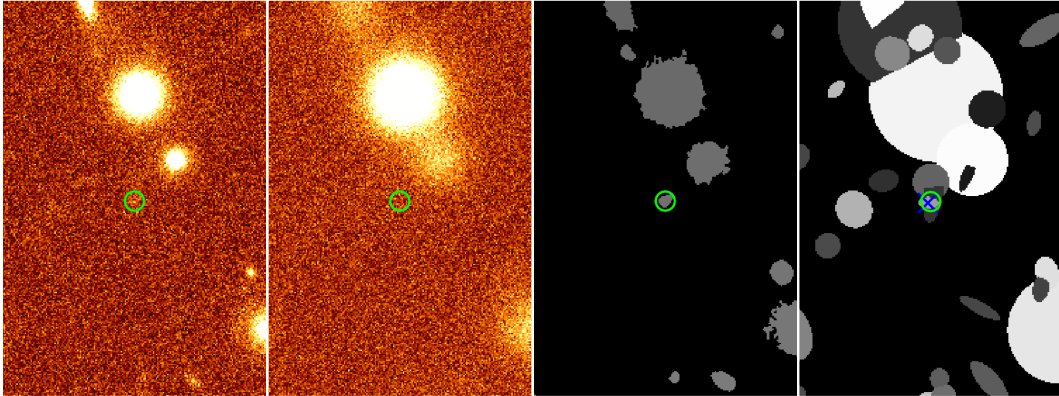
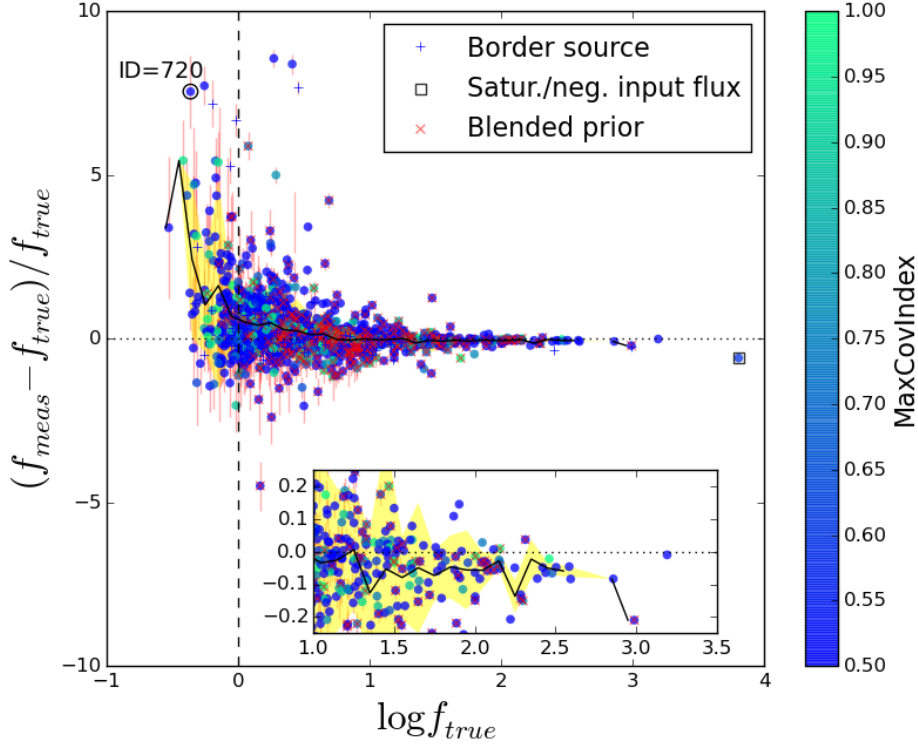


**Figure 11.** Accuracy of the flux determination in a simulation containing extended objects, overlapping priors and SETRACTOR detection. Top: relative flux difference  $(f_{meas} - f_{input})/f_{input}$  versus logarithm of the input flux  $f_{input}$  for a simulated image populated with extended sources (FWHM=1.66"). Symbols and colors are as in Fig. 9. The inner panel shows a magnification of the brighter end of the distribution. The outlier marked with the open black circle, ID=720, is shown in the bottom panel: left to right, HRI (FWHM=0.2"), LRI, SETRACTOR segmentation map and "true" segmentation map. The green circles show the object detected via SETRACTOR, while the blue cross shows its "true" position. See text for more details.

neighbors blending in the LRI. This causes a global underestimation of the errors.

To check the performance of T-PHOT at FIR wavelengths, we also run a test on a simulated Herschel SPIRE 250  $\mu\text{m}$  image (FWHM=25", 3.6" pixel scale). The simulated image (shown alongside with the obtained residuals in Fig. 4) mimics real images from the GOODS-Herschel program, the deepest Herschel images ever obtained. This image was produced with the technique presented in Leiton et al. (2015): we first derived (predicted) flux densities for all the 24  $\mu\text{m}$  detections ( $F_{24\mu\text{m}} > 20\mu\text{Jy}$ ) in GOODS-North, which are dependent on their redshift and flux den-

sities at shorter wavelengths, and then we injected these sources into the real noise maps from GOODS-Herschel imaging. Additional positional uncertainties, typically 0.5", were also applied to mimic real images. As shown in Leiton et al. (2015), these simulated images have indeed similar pixel value distribution as real images (see also Wang et al. 2015, for more details). For this test, T-PHOT was run using the list of all the 24  $\mu\text{m}$  sources as unresolved priors. The results of the test are plotted in Fig. 13, and they show that even in this case T-PHOT can recover the input fluxes of the sources with great statistical accuracy (the mean of the relative deviation from the expected measurements, i.e.

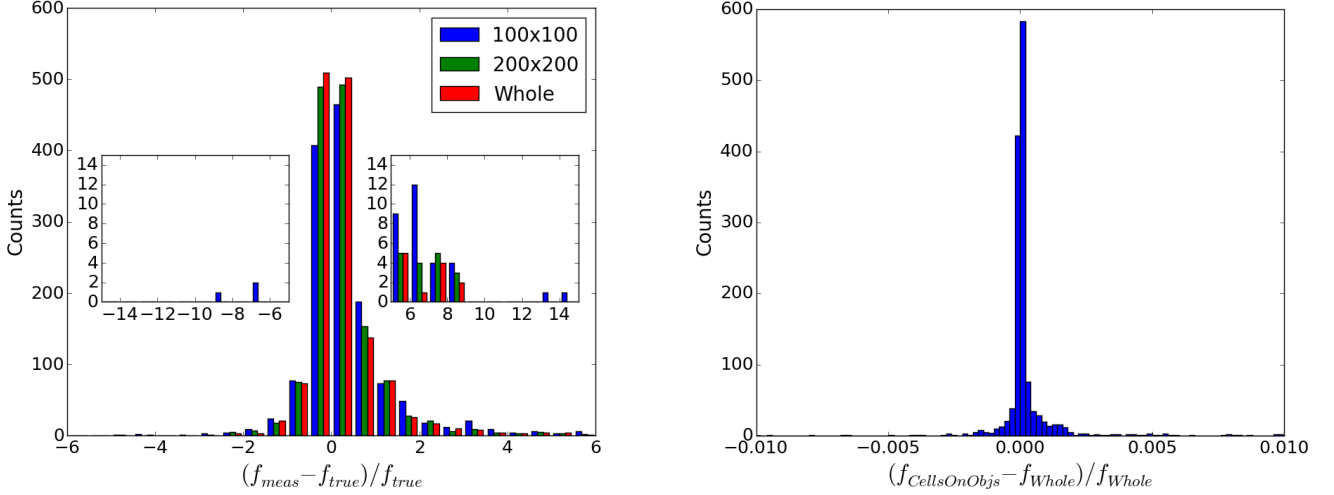


**Figure 12.** Accuracy of the flux determination. Top panel: for the same simulation described in Fig. 11, the histograms show the results for three different fitting methods: regular grid  $100 \times 100$  pixels (standard TFIT approach), regular grid  $200 \times 200$ , single fit on the whole image. The small boxes show the extended wings of the histograms, magnified for better viewing. The accuracy increases enlarging the cells and, reaches the best result with the single fit on the whole image. Bottom panel: the histogram shows the relative measured flux difference between the single fit on the whole image and the *cells-on-objects* method. Differences above 1% are very rare.

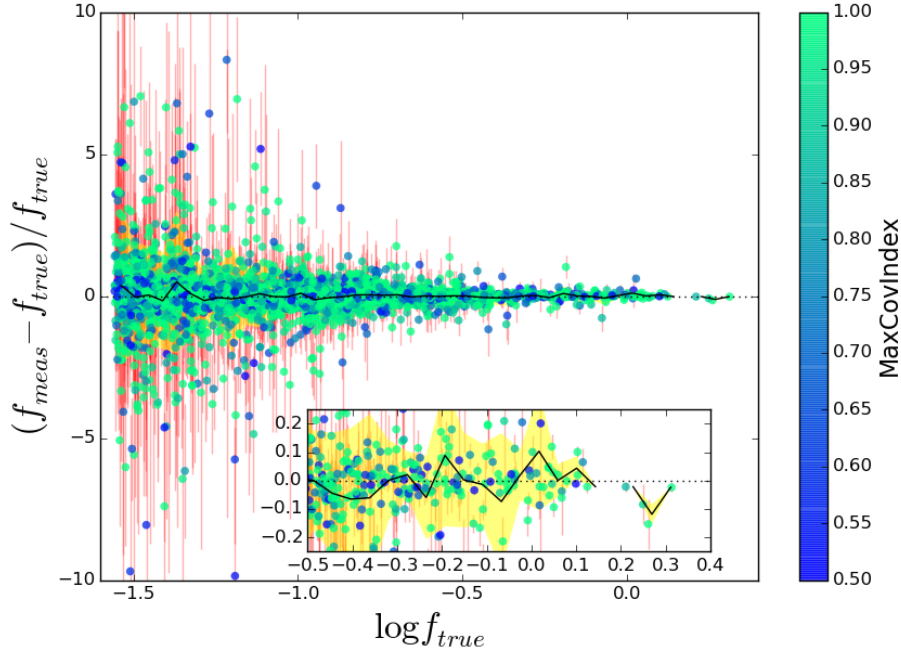


**Figure 13.** Accuracy of the flux determination in a FIR-like simulation (Herschel SPIRE  $250 \mu\text{m}$ ,  $\text{FWHM}=25''$ ,  $3.6''$  pixel scale), using unresolved priors. The symbols have the same meaning as in Fig. 11. See text for more details.

the black solid line in the plot, is consistent with zero down to the faintest fluxes). The results prove to be equivalent to those obtained on the same datasets with other public software specifically developed for FIR photometry, such as FASTPHOT (B  thermin et al. 2010).

#### 4.1.3. Testing different fitting options: cell dimensions

We then proceeded to check the performance of the different fitting techniques that can be used in T-PHOT. To this aim, we repeated the test on the  $1.66''$  LRI with extended priors and SEXTRACTOR priors, described in Sect. 4.1.2, with different fitting methods: using a regular grid of cells of  $100 \times 100$  pixels, a regular grid of cells of  $200 \times 200$  pixels, and the *cells-on-objects* method, comparing the results with those from the fit of the whole image at once.

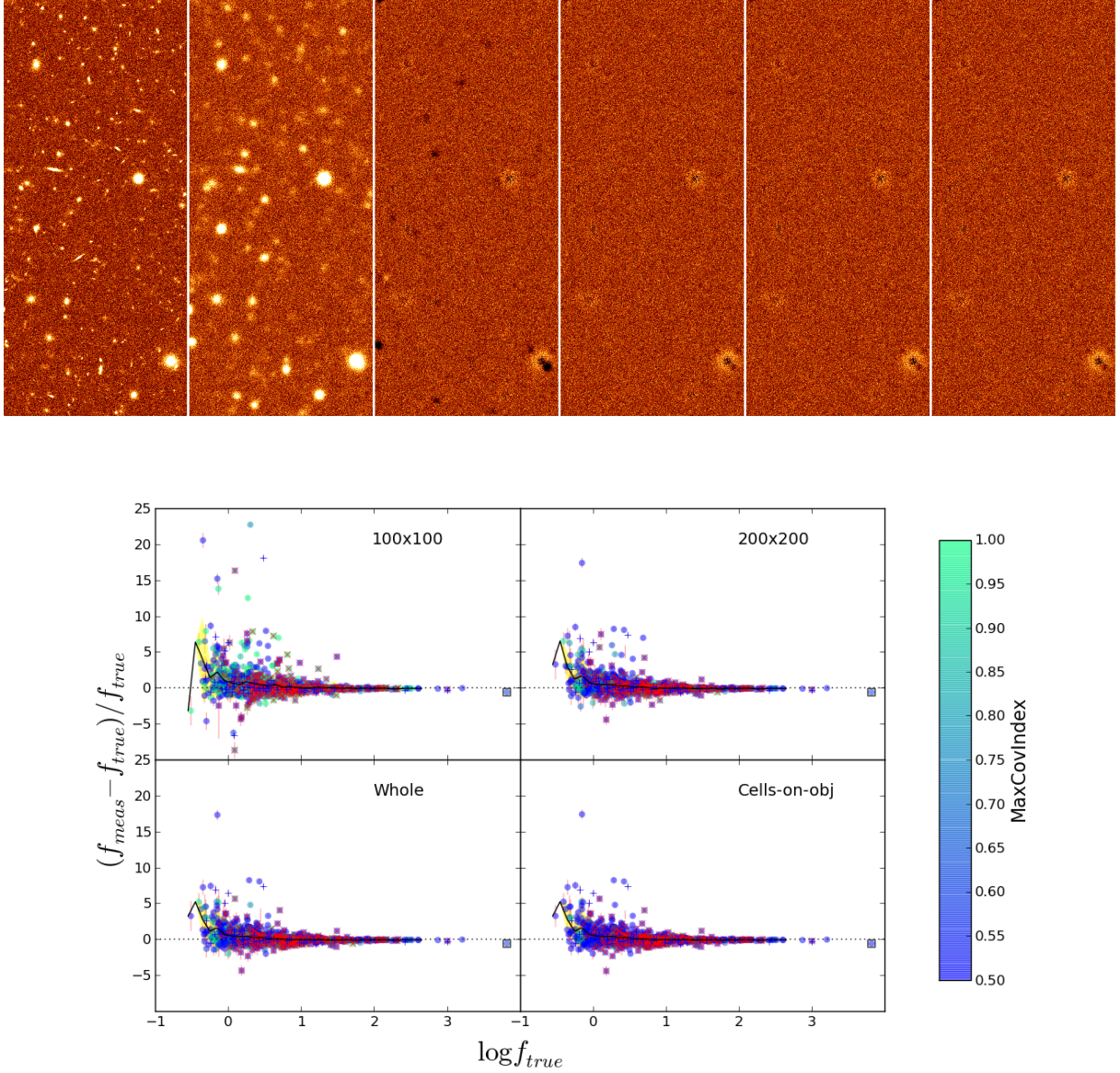


**Figure 14.** Accuracy of the flux determination. For the same simulation described in Fig. 11, the plots show the results for four different fitting methods. Top panel, left to right: HRI (FWHM=0.2''), LRI (FWHM=1.66''), residuals using a regular grid of  $100 \times 100$  pixels cells (standard TFIT approach), a regular grid of  $200 \times 200$  pixels cells, a single fit on the whole image, and the *cells-on-objects* method. The spurious fluctuations in the last two panels are due to segmentation inaccuracies, as in Fig. 11. Bottom panels, left to right and top to bottom: relative measured flux differences with respect to true fluxes, same order as above. Note that the values of the covariance index are different in each case, because of the varying sizes of the cells (and therefore of the relative matrix).

The results of the tests are shown in Figs. 12 and 14. The first figure compares the distributions of the relative errors in measured flux for the runs performed on the  $100 \times 100$  pixels grid, on the  $200 \times 200$  pixels grid, and on the whole image at once. Clearly, using any *regular* grid of cells worsens the results, as anticipated in Sect. 2.1.5. Enlarging the sizes of the cells yields improvement, but does not completely solve the problem. Note that the adoption of an arbitrary grid of cells of any dimension in principle is prone to the introduction of potentially large errors, because (possibly bright) contaminating objects may contribute to the brightness measured in the cell, without being included as contributing sources. A mathematical sketch of this issue is explained in the Appendix (and see also Sect. 4.2).

The second histogram compares the differences between the fit on the whole image and the one with the *cells-on-objects* method. Almost all the sources yield identical results with the two methods, within  $(f_{meas} - f_{true})/f_{true} < 0.001$ . This proves how the *cells-on-objects* method can be considered a reliable alternative to the single fit method.

Fig. 14 compares the HRI, the LRI, and the residual images obtained with the four methods and their distributions of relative errors, showing quantitatively the difference between the analyzed cases.

In summary, it is clear that an incautious choice of cell size may lead to unsatisfactory and catastrophic outcomes. On the other hand, the advantages of using a single fit, and the equivalence of the results obtained with the sin-

gle fit and the *cells-on-objects* technique, are evident. As already anticipated, one should bear in mind that the *cells-on-objects* method is only convenient if the overlapping of sources is not dramatic, as in ground-based optical observations. For IRAC and FIR images, on the other hand, the extreme blending of sources would cause the cells to be extended over regions approaching the size of the whole image, so that a single fit would be more convenient, although often still CPU-time consuming.

#### 4.1.4. Testing different fitting options: threshold fitting

As described in Sect. 2.1.5, T-PHOT includes the option to impose a lower threshold on the normalized fluxes of templates so as to exclude from the fit low signal-to-noise pixels. Fig. 15 shows a comparison of the relative errors obtained with three different values of the THRESHOLD parameter:  $t = 0$ ,  $t = 0.5$  and  $t = 0.9$  (this means that only pixels with normalized flux  $f_{norm} > t \times f_{peak}$  in the convolved template will be used in the fitting procedure). The differences are quite small, however a non-negligible global effect can be noticed: all sources tend to slightly decrease their measurement of flux when using a threshold limit. This brings faint sources (generally overestimated without using the threshold) closer to their “true” value, at the same time making bright sources too faint. This effect deserves careful investigation which is beyond the scope of this study, and is postponed to a future paper.

#### 4.1.5. Colors

A final test was run introducing realistic colors, i.e. assigning fluxes to the sources in the LRI consistent with a realistic SED (as output by GENCAT, see Sect. 4.1.2), instead of imposing them to be equal to the HRI fluxes. We took IRAC-ch1 as a reference filter for the LRI, consistently with the chosen FWHM of 1.66”. Furthermore, we allowed for variations in the bulge-to-disc ratios of the sources to take into account possible effects of color gradients. We compared the results obtained with T-PHOT with the ones obtained with two alternative methods to determine the magnitudes of the sources in the LRI: namely, SExtractor dual mode aperture and MAG\_BEST photometry (with HRI as detection image). The differences between measured and input magnitudes in the LRI,  $m_{meas} - m_{true}$ , are plotted in Fig. 16. Clearly, T-PHOT ensures the best results, with much less scattered measurements than both the other two methods, and very few outliers.

#### 4.2. Performance on real datasets

It is instructive to check how T-PHOT performs on real datasets, in addition to simulations. To this aim, we run two different tests. In the first, we compared the results of the TFIT CANDELS analysis on the UDS CANDELS I-band (Galametz et al. 2013) to a T-PHOT run obtained using the *cells-on-objects* method and different parameters in the kernel registration stage. Fig. 17 shows the histograms of the differences in the photometric measurements between TFIT and T-PHOT. Many sources end up with a substantially different flux, because of the two cited factors (a better kernel registration and the different fitting procedure). Note that the majority of the sources have *fainter* fluxes

with respect to the previous measurements, precisely because of the effect described in Sect. 4.1.2: fitting using a grid of cells introduces systematic errors assigning light from sources which are not listed in a given cells but overlap with it to the objects recognized as belonging to the cell. To further check this point, Fig. 18 shows some examples of the difference between the residuals obtained with TFIT (official catalog) and those obtained with this T-PHOT run using *cells-on-objects* method, also introducing better registration parameters in the *dance* stage. Clearly, the results are substantially different, with many black spots (sources with spurious overestimated fluxes) disappearing. Also, the registrations appear to be generally improved.

The second test was run on FIR/sub-mm SCUBA-2 (450  $\mu\text{m}$ , FWHM=7.5”) and Herschel (500  $\mu\text{m}$ , FWHM=36”) images of the COSMOS-CANDELS field. In both cases, a list of 24+850  $\mu\text{m}$  sources was used as unresolved priors. Fig. 19 shows the original images on the top row, and the residuals on the bottom row. The model has removed all significant sources from the 450  $\mu\text{m}$  map and the majority from the 500  $\mu\text{m}$  map. Fig. 20 shows a comparison of the fluxes measured in the T-PHOT fits to the 450  $\mu\text{m}$  and 500  $\mu\text{m}$  maps at 24+850  $\mu\text{m}$  prior positions, with the error bars combining the errors on both flux measurements. Agreement within the errors implies successful deconvolution of the Herschel image to reproduce the fluxes measured in the higher-resolution SCUBA-2 image. This typology of analysis is very complex and we do not want to address here the subtleties of the process; we refer the reader to Wang et al. (2015, in preparation) and Bourne et al. (2015, in preparation) for detailed discussions on the definition of a robust and reliable approach to measure FIR and sub-mm fluxes. These simple tests, however, clearly show that T-PHOT is successful at recovering the fluxes of target sources even in cases of extreme confusion and blending, within the accuracy limits of the method.

## 5. Computational times

As anticipated, T-PHOT ensures a large saving of computational times compared to similar codes like TFIT and CONVPHOT, when used with identical input parameters. For example, a complete, double-pass run on the whole CANDELS UDS field at once (I band;  $\sim 35000$  prior sources; LRI  $30720 \times 12800 = 400$  million pixels; standard TFIT parameters and grid fitting) is completed without memory swaps in ca. 2 hours (i.e., 1 hour per pass) on a standard workstation (INTEL i5, 3.20 GHz, RAM 8 Gb). A complete, double pass run on the GOODS-S Hawk-I W1 field ( $\sim 17500$  prior sources, LRI  $10700 \times 10600 = 100$  millions pixels, identical parameters) is completed in  $\sim 20$  minutes. For comparison, TFIT may require many hours ( $\sim 24$ ) to complete a single pass on this Hawk-I field on the same machine. It must be said that TFIT by default produces cutouts and templates for all the sources in the HRI image; selecting the ones belonging to the LRI field and inputting an ad-hoc catalog would have reduced the computing time, say by a factor of two (i.e., 11 hours for the a single pass). It was not possible to process large images like the UDS field in a single run, because of RAM memory failing. CONVPHOT timings and memory problems are similar to the TFIT ones, although due to different causes (being written in C, computation is generally faster, but it employs a slower convolution method and the solution of the linear system

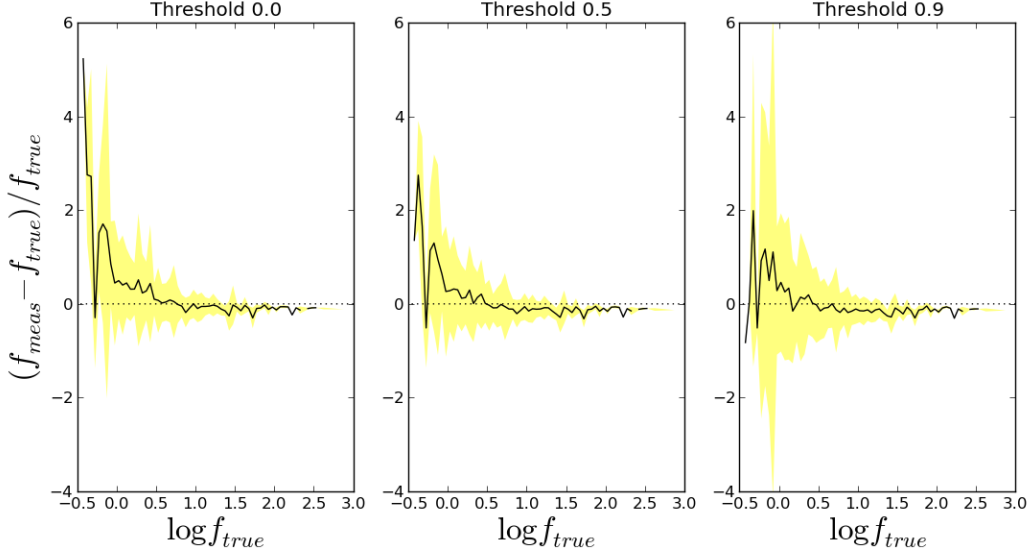


**Figure 15.** Effects of threshold fitting (Sect. 4.1.4). Mean relative error (black line) and standard deviation (yellow shaded area) for three simulations with different threshold values (0.0, 0.5, 0.9). Only pixels with normalized flux higher than the threshold values are included in the fit. Larger threshold values result in more accurate measurements for faint sources, at the expense of a systematic underestimation of the flux for brighter ones.

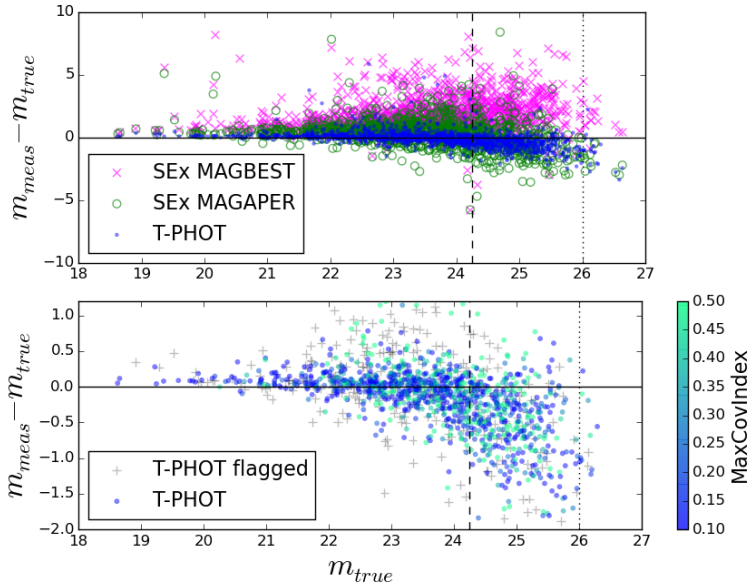


**Figure 16.** Top: measured magnitude differences ( $m_{meas} - m_{true}$ ) versus “true” input magnitudes  $m_{true}$ , for a couple of simulated images populated with extended sources (HRI has FWHM=0.2” and HST  $H$ band-like fluxes, LRI has FWHM=1.66” and IRACch1-like fluxes), using three different methods: SEXTRACTOR dual-mode aperture, SEXTRACTOR dual-mode “best”, and T-PHOT. Vertical lines show the  $5\sigma$  (dashed) and  $1\sigma$  (dotted) limits of the simulated LRI. Bottom: magnification of the top panel, showing only T-PHOT results, color-coded as a function of the covariance index. See text for more details.

in performed as a single fit instead of grid fitting like in TFIT, being much more time consuming).

Adopting the *cells-on-objects* (Sect. 2.1.5) method increases the computational time with respect to the TFIT standard cell approach, but it is still far more convenient than the CONVPHOT standard single fit approach, and gives nearly identical results.

Table 2 summarizes the computational times for an extended tests on a set of simulated images having different detection depths (and therefore number of sources) and dimensions, with LRI FWHM=1.66”. The simulations have been run on the same machine described above, using three different methods: whole image fitting, *cells-on-objects* and  $100 \times 100$  pixels cells fitting.

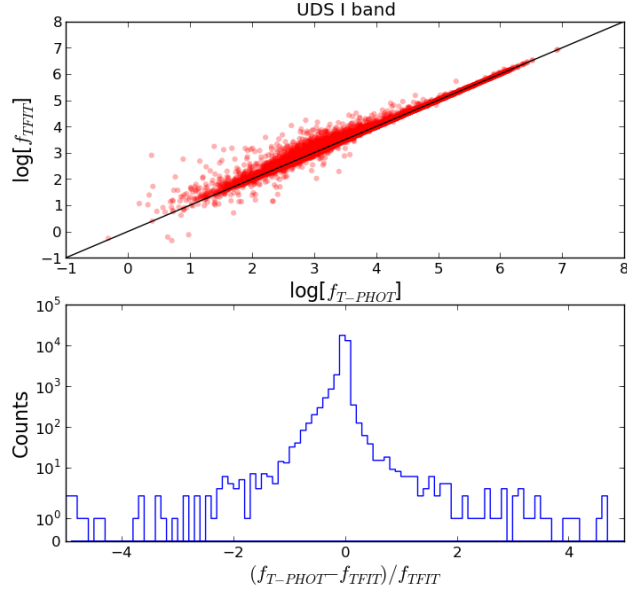


**Figure 17.** UDS I band TFIT vs. T-PHOT comparison. Top panel: compared measured fluxes. Bottom panel: histogram of relative measured flux difference.

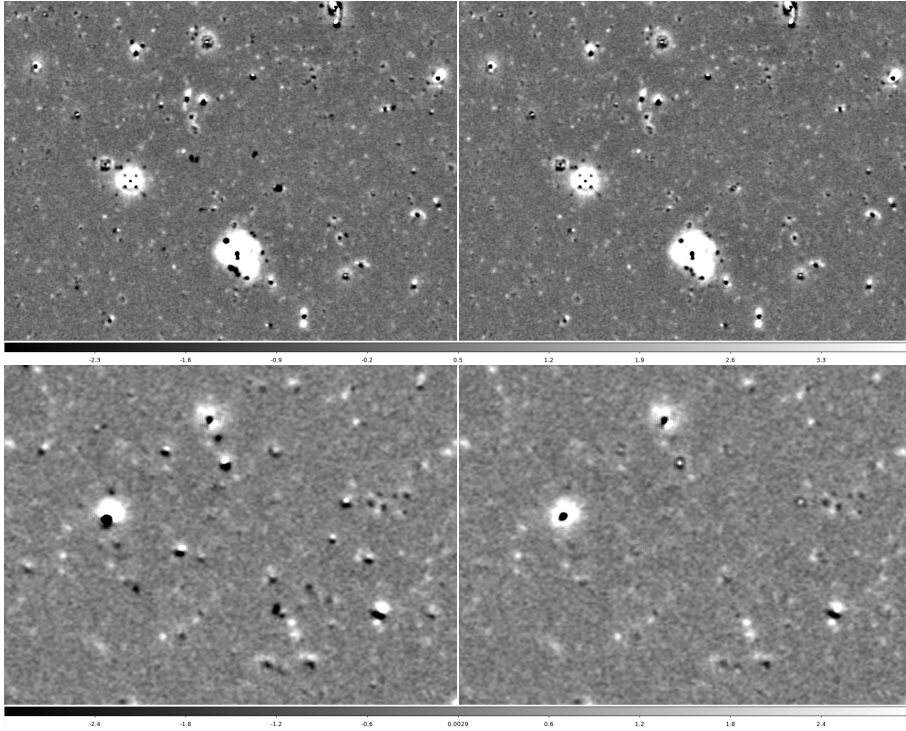


**Figure 18.** UDS I band TFIT vs. T-PHOT comparison. The panels on the left show two small patches of the “official” CANDELS residual image obtained using T-FIT. The residual images of the same regions are showed in the right panels, this time obtained using T-PHOT with *cells-on-objects* method and improved local kernel registration. Note the disappearance of many spurious black spots.

## 6. Summary and conclusions

We have presented T-PHOT, a new software package developed within the ASTRODEEP project. T-PHOT is a robust and versatile tool, aimed at the photometric analysis of deep extragalactic fields at different wavelengths and spa-

tial resolution, deconfusing blended sources in low resolution images.

T-PHOT uses priors obtained from a high resolution detection image to obtain normalized templates at the lower resolution of a measurement image, and minimizes a  $\chi^2$  problem to retrieve the multiplicative factor relative to each source, which is the searched quantity, i.e. the flux in the

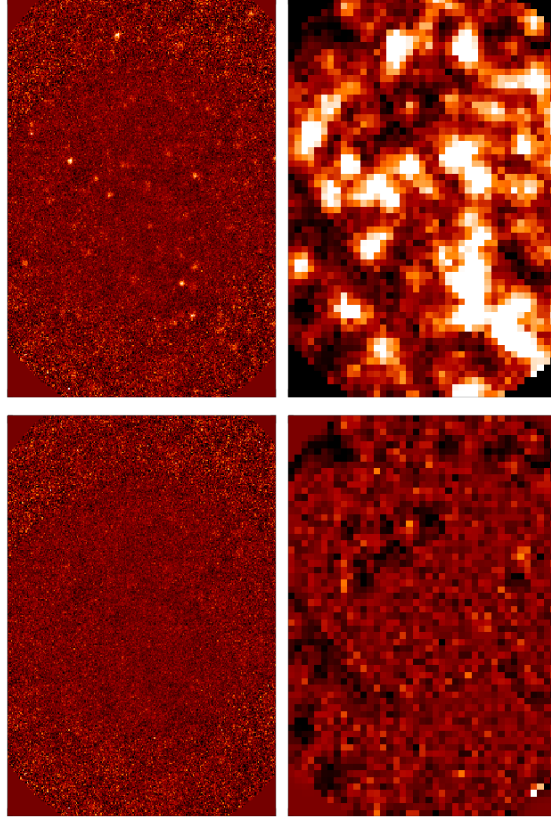


**Figure 19.** Results from a test run using T-PHOT with unresolved priors on FIR/sub-mm real dataset. Upper row, left to right: SCUBA-2 450  $\mu\text{m}$  (FWHM=7.5'') and Herschel 500  $\mu\text{m}$  (FWHM=36'') images of the COSMOS-CANDELS fields. Lower row, left to right: residuals for the two fields, obtained with T-PHOT runs using a list of 24+850  $\mu\text{m}$  priors. See text for details.

Size[pix] \ $\text{mag}_{lim,det}$	27	28	29
<b>Number of sources</b>			
2500 $\times$ 2500	523	1070	1398
5000 $\times$ 5000	2104	4237	5561
10000 $\times$ 10000	8390	16807	22394
20000 $\times$ 20000	33853	65536	65536
<b>Whole image fitting</b>			
2500 $\times$ 2500	38'' (2'')	54'' (10'')	1'9'' (20'')
5000 $\times$ 5000	3'26'' (1'1'')	11'9'' (7'41'')	20'28'' (16'1'')
10000 $\times$ 10000	1h28'22'' (1h15'46'')	8h26'1'' (7h58'10'')	21h16'24'' (20h27'53'')
20000 $\times$ 20000	-	-	-
<b>Cells-on-objects fitting</b>			
2500 $\times$ 2500	46'' (4'')	1'11'' (16'')	1'30'' (33'')
5000 $\times$ 5000	3'1'' (18'')	4'27'' (1'8'')	6'3'' (2'20'')
10000 $\times$ 10000	12'27'' (1'12'')	17'52'' (4'31'')	25'11'' (9'52'')
20000 $\times$ 20000	51'12'' (6'1'')	1h34'40'' (35'8'')	1h43'10'' (41'2'')
<b>100<math>\times</math>100 pixels cells fitting</b>			
2500 $\times$ 2500	52'' (3'')	1'6'' (7'')	1'14'' (9'')
5000 $\times$ 5000	3'16'' (14'')	4'22'' (29'')	4'54'' (41'')
10000 $\times$ 10000	13'4'' (56'')	17'12'' (1'54'')	19'47'' (2'53'')
20000 $\times$ 20000	55'24'' (6'19'')	1h18'38'' (15'53'')	1h17'17'' (17'58'')

**Table 2.** Computational times test for T-PHOT runs on images of given dimensions and limiting magnitude in detection. Each entry of the table reports the total duration of run, the duration the fitting stage alone between parentheses, and the number of fitted sources. The **dance** stage takes most of the CPU time after the fitting routine.

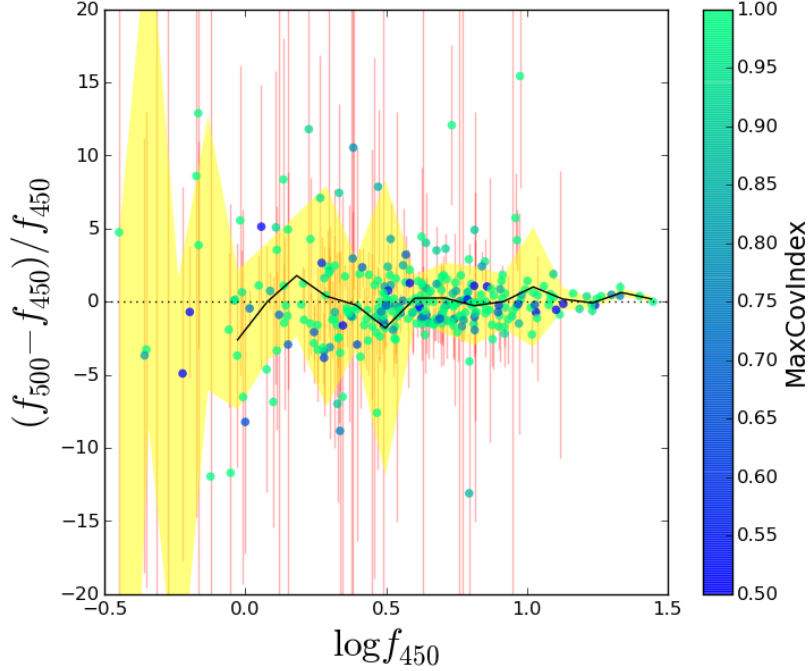


**Figure 20.** Accuracy of the flux determination for the dataset described in Fig. 19: measured Herschel 500  $\mu\text{m}$  (FWHM=36 $''$ ) fluxes  $f_{500}$  are compared to the fluxes obtained for the SCUBA-2 450  $\mu\text{m}$  (FWHM=7.5 $''$ )  $f_{450}$ , considered as reference fluxes (using 24+850  $\mu\text{m}$  unresolved priors in both cases). The symbols have the same meaning as in Fig. 11; the error bars now include the measured error on the reference flux. See text for more details.

LRI. The priors can be either real cutouts from the HRI, or a list of positions to be fitted as PSF-shaped sources, or analytical 2-d models, or a mix of the three types. Different options for the fitting stage are given, including a *cells-on-objects* method which is computationally efficient while yielding accurate results for relatively small FWHMs. T-PHOT ensures a large saving of computational time as well as increased robustness with respect to similar public codes like its direct predecessors TFIT and CONVPHOT. With an appropriate choice of the parameter settings, greater accuracy is also achieved.

As a final remark, it should be pointed out that the analysis presented in this work deals with idealized situations, namely simulations or comparisons with the performances of other codes on real datasets. There are a number of subtle issues regarding complex aspects of the PSF-matching technique, which become of crucial importance when working on real data. A simple foretaste of such complexity can be obtained considering the problem described in Sect. 4, i.e. the correct amplitude to be assigned to the segmented area of a source. Work is ongoing on this, and the full discussion will be presented in a subsequent companion paper.

As we have shown, T-PHOT proves to be an efficient tool for the photometric measurements of images on a very broad range of wavelengths, from UV to sub-mm, and is currently being routinely used by the ASTRODEEP community to analyse data from different surveys (e.g. CANDELS, Frontier Fields, AEGIS). Its main advantages with respect to similar codes like TFIT or CONVPHOT can be summarized as follows:

- when used with the same parameter settings of TFIT, T-PHOT is many times faster (up to hundreds of times),

and the same can be said with respect to other similar codes (e.g., CONVPHOT);

- T-PHOT is more robust, more user-friendly, and can handle larger datasets thanks to an appropriate usage of the RAM;
- T-PHOT can be used with three different types of priors (real high-resolution cutouts, analytical models and/or unresolved point sources) making it a versatile tool for the analysis of different datasets over a wide range of wavelengths from UV to sub-mm;
- T-PHOT offers many options to perform the fit in different ways, and with an appropriate choice of parameter settings it can give more accurate results.

Future applications might include the processing of EUCLID and CCAT data. New releases of the software package, including further improvements and additional options, are planned for the next future.

*Acknowledgements.* The authors acknowledge the contribution of the FP7 SPACE project ASTRODEEP (Ref.No: 312725), supported by the European Commission. JSD acknowledges the support of the European Research Council via the award of an Advanced Grant. FB acknowledges support by FCT via the postdoctoral fellowship SFRH/BPD/103958/2014 and also the funding from the programme UID/FIS/04434/2013. RJM acknowledges the support of the European Research Council via the award of a Consolidator Grant (PI McLure). The authors would like to thank Kuang-Han Huang, Mimi Song, Alice Mortlock and Michal Michalowski, for constructive help and suggestions, and the anonymous referee for useful advice.

## References

- Agüeros, M. A., Ivezić, Ž., Covey, K. R., et al. 2005, *AJ*, 130, 1022  
 Bertin, E. 2009, *Mem. Soc. Astron. Italiana*, 80, 422

B ethermin, M., Dole, H., Cousin, M., & Bavouzet, N. 2010, *A&A*, 516, A43

Bourne, N., Dunlop, J., Bruce, V., et al. 2015

Daddi, E., Cimatti, A., Renzini, A., et al. 2004, *ApJ*, 617, 746

Davis, T. A. 2006, *Direct Methods for Sparse Linear Systems* (SIAM, Philadelphia, PA)

De Santis, C., Grazian, A., Fontana, A., & Santini, P. 2007, *New A*, 12, 271

Elbaz, D., Dickinson, M., Hwang, H. S., et al. 2011, *A&A*, 533, A119

Fontana, A., Santini, P., Grazian, A., et al. 2009, *A&A*, 501, 15

Galametz, A., Grazian, A., Fontana, A., et al. 2013, *ApJS*, 206, 10

Grogin, N. A., Kocevski, D. D., Faber, S. M., et al. 2011, *ApJS*, 197, 35

Guo, Y., Ferguson, H. C., Giavalisco, M., et al. 2013, *ApJS*, 207, 24

Laidler, V. G., Papovich, C., Grogin, N. A., et al. 2007, *PASP*, 119, 1325

Leiton, R., Elbaz, D., Okumura, K., et al. 2015, *ArXiv e-prints*

Obri c, M., Ivezi c,  ., Best, P. N., et al. 2006, *MNRAS*, 370, 1677

Roseboom, I. G., Oliver, S. J., Kunz, M., et al. 2010, *MNRAS*, 409, 48

Schreiber, C., Merlin, E., Elbaz, D., et al. 2015

Shu, X., Merlin, E., Elbaz, D., et al. 2015

Stetson, P. B. 1987, *PASP*, 99, 191

Wang, L., Viero, M., Clarke, C., et al. 2014, *MNRAS*, 444, 2870

Wang, T., Schreiber, C., Elbaz, D., et al. 2015

```
# T-PHOT PARAMETER FILE

# PIPELINE

# 1st pass
order standard
#priors, convolve, fit, diags, dance, plotdance

# PRIORS STAGE

# Choose priors types in use:
usereal True
usemodels True
useunresolved True

# Real 2-d profiles
hiresfile      HRI.fits
hirescat       HRI.cat
hiresseg       HRI.seg.fits
normalize       true
subbckg True
savecut true
cutoutdir      cutouts
cutoutcat      cutouts/_cutouts.cat

# Analytical 2-d models
modelscat models/models.cat
modelsdir models

culling false

# Unresolved point-like sources
poscat pos.cat
psffile psf.fits

# CONVOLUTION STAGE

loresfile      LRI.fits
loreserr       LRI.rms.fits
errtype        rms
rmsconstant    1
relscale       1

FFTconv true
multikernels   false
kernelfile     kernel.fits
kernellookup   ch1_dancecard.txt

templatedir    templates
templatecat    templates/_templates.cat

# FITTING STAGE

# Filenames:
fitpars        tpipe_tphot.param
tphotcat       lores_tphot.cat_pass1
tphotcell      lores_tphot.cell_pass1
tphotcovar     lores_tphot.covar_pass1
```

## Appendix A: The parameter file

Below is a template of the standard first pass parameter file to be given as input to T-PHOT (similar templates for both the first and the second pass are included in the downloadable tarball). It is very similar to the original TFIT parameter file, and part of the description is directly inherited from it.

### A.1. Pipeline

Standard optical/NIR double-pass runs can be achieved setting `order standard` and `order standard2`.

A standard first pass run includes the stages `priors`, `convolve`, `fit`, `diags`, `dance`, `plotdance`. The stage `priors` allows for an automatic re-construction of the pipeline depending on the input data given in the following sections (see the documentation included in the tarball). A standard second pass run includes the stages `convolve`, `fit`, `diags`, `archive`. The `archive` stage creates a directory after the name of the LRI, with some specifications, and archives the products of both runs.

FIR/sub-mm double-pass runs can be achieved setting `order positions`, `fit`, `diags`, `dance`, `plotdance` and `order positions`, `fit`, `diags`, `archive`.

### A.2. Priors

Each prior must have an *unique* identificative number (ID) to avoid errors. The user must be careful to give the correct information in this paramfile. Select the priors to be used by switching on/off the relative keywords: `usereal`, `usemodels`, `useunresolved`.

- `hiresfile`: the high resolution, detection image. If a catalog and a segmentation map are given in the two subsequent entries (`hirescat` and `hiresseg`), cutouts will be created out of this image. It is necessary if a catalog of real or model priors are be used. The catalog `hirescat` must be in a standard format: `id x y xmin ymin xmax ymax background SEx_flux`. (`x` and

`y` are the coordinates of the source in HRI pixel reference frame, `xmin` `ymin` `xmax` `ymax` are the limits of the segmentation relative to the source in HRI pixel reference frame, `background` is the value of the local background and `SEx_flux` is a reference isophotal flux).

- `poscat`: a catalog of positions for unresolved, point-like sources. No HRI image/segmentation are needed, while the PSF to be used to create the models is mandatory

```

# Control parameters:
fitting coo
cellmask      true
maskfloor     1e-9
writecovar    true

threshold 0.0
linsyssolver lu
clip false

# DIAGNOSTICS STAGES

modelfile     lores_collage_pass1.fits

# Dance:
dzonesize    100
maxshift     1.0
ddiagfile    ddiags.txt
dlogfile     dlog.txt
dancefft     false

```

(psffile). The catalog must be in the standard format `id x y`.

- **modelscat**: a catalog (with format `id x y xmin ymin xmax ymax background SExflux`, as for a standard HRI priors catalog) of model priors. `modelmdir` is the directory in which the stamps of the models are stored. Models with two or more components can be processed, but each component must be treated as a separated object, with a different ID, and a catalog for each component must be given. Catalogs for each component must have the same name, but ending with `"_1"`, `"_2"` etc.; put the `"_1"` catalog in the paramfile. *Note that two components of the same object should not have exactly identical positions, to avoid numerical divergencies.*
- **culling**: if `True`, objects in the catalog (real priors and/or models) but not falling into the LRI frame will not be processed; if it is false, all objects in the catalog will be processed (useful for storing cutouts for future reuse on different datasets) and the selection of objects will be done before the convolution stage.
- **subbckg**: if `True`, subtract the value given in the input catalog from each cutout stamp.
- **cutoutdir**: the directory containing the cutouts.
- **cutoutcat**: the catalog of the cutouts, containing the flux measured within the cutout area (which may be different from the `SExflux` given in the input catalog, e.g. if the segmentation has been dilated). Note that these are output parameters if you start from the `priors/cutout` stage; they are input parameters for the convolve stage.
- **normalize**: determines whether the cutouts will be normalized or not; it is normally set to true, so that the final output catalog will contain fluxes, rather than colors.

### A.3. Convolution

- **loresfile**, **loreserr**: the LRI and RMS images. T-PHOT is designed to work with an RMS map as the error map, but it will also accept a weight map, or a single constant value of the RMS from which an RMS map is generated. The `errtype` specifies which kind of error image is provided. For best results, use a source-

weighted RMS map, to prevent the bright objects from dominating the fit.

- **relscale**: the relative pixel scale between the two images. For example if the HRI has a pixel scale of 0.1 arcsec/pixel and the LRI has a pixel scale of 0.5 arcsec/pixel, the value of `relscale` should be 5. If the LRI has been manipulated to match the HRI pixel scale and WCS data (e.g. using codes like SWARP by E. Bertin), put `relscale 1`.
- **kernelfile**: the convolution kernel file. The kernel must be a FITS image on the same pixel scale as the high res image. It should contain a centered, normalized image.
- **FFTconv** is `True` if the convolution of cutouts with the smoothing kernel is to be done in Fourier space (via FFTW3).
- **kerntxt** may be explicitly put `True` if one wishes to use a text file containing the kernel instead of a `.fits` one. T-PHOT supports the use of multiple kernels to accommodate a spatially varying PSF. To use this option, set the `multikernels` value to true, and provide a `kernellookup` file (it is automatically produced during the `dance` stage in the first pass, but it can also be fed externally) that divides the LRI into rectangular zones, specified as pixel ranges, and provides a local convolution kernel filename for each zone. Any objects which fall in a zone not included in the lookup file will use the transfer kernel specified as `kernelfile`.
- **templatedir**: the directory containing the templates created in the convolve stage, listed in the catalog `templatecat`. Note that these are output parameters for the convolve stage, and an input parameter for all subsequent stages.

### A.4. Fitting stage

- **fitpars**, **tphotcat**, **tphotcell**, **tphotcovar**: these are all output parameters. The `tfitpars` file specifies the name of the special parameter file for the fitting stage that will be generated from the parameters in this file. The others are filenames for the output catalog, cell, and covariance files, respectively.
- **fitting**: this keyword tells T-PHOT which method to use to perform the fitting (see also Appendix B):
  - `coo` or `0` for *cells-on-objects*;
  - `single` or `-1` for single fit;
  - `single!` or `-10` for optimized single fit (the LRI is divided in square cells containing roughly 10000 sources each);
  - `cell_xdim`, `cell_ydim`, `cell_overlap` for arbitrary grid of cells.
- **cellmask**: if `true`, uses a mask to exclude pixels from the fit which do not contain a value of at least `maskfloor` in at least one template.
- **writecovar**: if `true`, writes the covariance information out to the `tphotcovar` file.
- **threshold**: forces to use a threshold on the flux, to only use the central parts of the objects.
- **linsyssolver**: the chosen solution method, i.e. LU, Cholesky or Iterative Biconjugate Gradient (IBG). LU is default.
- **clip**: tells whether to loop on the sources excluding negative solutions.

### A.5. Diagnostic stages

- **modelfile**: the `.fits` file that will contain the collage made by multiplying each template by its best flux and dropping it into the right place. An additional diagnostic file will be created: it will contain the difference image (`LRI - modelfile`). Its filename will be created by prepending `resid_` to the `modelfile`.
- **dzonesize** specifies the size of the rectangular zones over which the pixels cross-correlation between LRI and `modelfile` will be calculated during the `dance` stage. It should be comparable to the size over which misregistration should be roughly constant; but, it must be large enough to contain enough objects to provide a good signal to the cross-correlation.
- **maxshift** specifies the maximum size of the `x,y` shift, in LRI pixel frame, which is considered to be valid. Any shift larger than this is considered spurious and dropped from the final results, and replaced by an interpolated value from the surrounding zones. Ideally,  $\text{maxshift} \simeq 1\text{pixel} \times \text{FWHM}_{LRI} / \text{FWHM}_{HRI}$ .
- **ddiagfile** is an output parameter for the `dance` stage, and an input parameter for the `plotdance` stage.
- **dlogfile** is an output parameter; it simply contains the output from the cross-correlation process.
- **danceFFT**: if `True` cross-correlation is to be performed using FFT techniques rather than in real pixels space.

## Appendix B: The cells-on-objects algorithm

Experiments on simulated images (see Sect. 4) clearly show that fitting small regions (cells) of the LRI, as done by default in TFIT, may lead to potentially large errors. This is particularly true if the dimensions of the cells are chosen to be smaller than an ideal size, which changes from case to case, and should however always be greater than  $\sim 10$  times the FWHM. However, it can be mathematically shown that the “arbitrary cells” method intrinsically causes the introduction of errors in the fit, as soon as a source is excluded from the cell (e.g., because its center is outside the cell) but contributes with some flux in some of its pixels.

Consider a cell containing  $N$  sources. For simplicity, assume that each source  $i$  only overlaps with the two neighbours  $i - 1$  and  $i + 1$ . Furthermore, assume that a  $(N + 1)$ -th source is contaminating the  $N$ -th source, but is excluded from the cell for some reason, for example (as in TFIT) because the centroid of the source lies outside the cell.

The linear system for this cell  $AF = B$  will consist of a matrix  $A$  with only the elements on the diagonal and those with a  $\pm 1$  offset as non-zero elements (a symmetric *band* matrix), and the vector  $B$  will contain the products of templates of each source with the real flux in the LRI (as a summation on all pixels), as described in Sect. 2.1.4. Given the above assumptions, this means that the  $N$ -th term of  $B$  will be higher than it should be (because it is contaminated by the external source).

Using the Cramer rule for the solution of squared linear systems, the flux for the object  $i$  is given by

$$f_i = \frac{\det A_i}{\det A} \quad (\text{B.1})$$

with  $A_i$  a square matrix in which the  $i$ -th columns is substituted with the vector  $B$ . If for example  $N = 3$ , for

$i = 1$  this gives

$$f_1 = [B_1(A_{22}A_{33} - A_{23}^2) - A_{12}(B_2A_{23} - B_3A_{22})] / \det A \quad (\text{B.2})$$

and since  $B_3$  is larger than it should,  $f_1$  will be overestimated (slightly, if  $A_{12}$  is not large, i.e. if sources 1 and 2 do not strongly overlap). On the other hand, for  $i = 3$  we have

$$f_3 = [A_{11}(A_{22}B_3 - A_{23}B_2) - A_{12}^2B_3 + B_1(A_{12}A_{23})] / \det A \quad (\text{B.3})$$

and in this case again  $A_{12}^2$  might be small, but the first term given by  $A_{11}A_{22}$  will be certainly large, resulting in catastrophic overestimation of  $f_3$ .  $f_2$  will of course be underestimated, as it would be easy to show.

From this simple test case it is clear that arbitrarily dividing the LRI into regions will always introduce errors (potentially non-negligible) in the fitting procedure, unless some method to remove dangerous contaminating sources is devised.

The *cells-on-objects* algorithm aims at ensuring the accuracy of the flux estimate while at the same time drastically decreasing computational times and memory requirements. As explained in Sect. 2.1.4, when this method is adopted a cell is centered around each detected source, and enlarged to include all its “potential” contaminant neighbors, and the contaminant of the contaminants, and so on. To avoid an infinite loop, the process of inclusion is interrupted when one of the following criteria is satisfied:

- the flux of the new neighbor is lower than a given fraction  $f_{flux}$  of the flux of the central object (the considered fluxes are: if real priors are used, the ones given in the HRI catalog; if unresolved priors are used, the ones read in the pixels of the LRI containing the coordinates of the sources; if analytical models are used, the ones of the models as reported in the HRI models catalog), or
- the template of the neighbor overlaps with its direct previous contaminant for a fractional area lower than  $f_{area}$ .

Experiments on simulations have shown that good results are obtained with  $f_{flux} = 0.9$  and  $f_{area} = 0.25$ , and these values are used as constants in the source code.

Note that if a cell is enlarged to more than 75% of the dimensions of the total LRI, T-PHOT automatically switches to the single fit on the whole image.

## Appendix C: Suggested best options

Of course, different problems require different approaches to obtain their best possible solution, and users are encouraged to try different options and settings. However, some indicative guidelines to optimize a run with T-PHOT can be summarized as follows.

- Be sure all the required input files exist, have correct format, and paths are correctly given in the parameter file.
- Whenever possible, fit the whole image at once (i.e. put `fitting single` in the parameter file). The more the sources, and the more severe their blending, the more CPU time will be required (see Sect. 5). If the blending is not dramatic, it’s safe to switch to the *cells-on-objects* method (i.e. put `fitting coo` in the parameter

file). On the other hand, if blending is severe this option would result in redundant fittings because cells would be enlarged to include as many as possible neighbors, increasing the total computing time. In this case, either stick to the whole image fitting, or (depending on the desired degree of accuracy) switch to the TFIT-like cells fitting.

- Spend some time in checking the output catalog, e.g. considering with caution fits relative to sources having flags  $> 0$  and covariance indices larger than 1.